frontiers | Frontiers in Physiology

TYPE Methods
PUBLISHED 24 September 2025
DOI 10.3389/fphys.2025.1635983

OPEN ACCESS

EDITED BY
Alexander V. Glushkov,
Odessa National Polytechnic University, Ukraine

REVIEWED BY
Josue Sznitman,
Technion Israel Institute of Technology, Israel
Rohin Banerji,
Boston University, United States

*CORRESPONDENCE
Neelesh A. Patankar,
n-patankar@northwestern.edu

RECEIVED 27 May 2025
ACCEPTED 28 August 2025
PUBLISHED 24 September 2025

CITATION
Chakravarty A, Kundu D, Panchagnula MV, Mohan A and Patankar NA (2025) Perspectives on physics-based one-dimensional modeling of lung physiology.
Front. Physiol. 16:1635983.
doi: 10.3389/fphys.2025.1635983

Perspectives on physics-based one-dimensional modeling of lung physiology

Aranyak Chakravarty[1,2], Debjit Kundu[2], Mahesh V. Panchagnula[2], Alladi Mohan[3] and Neelesh A. Patankar[4]*

[1]School of Nuclear Studies and Application, Jadavpur University, Kolkata, India, [2]Department of Applied Mechanics and Biomedical Engineering, Indian Institute of Technology Madras, Chennai, India, [3]Department of Medicine, Sri Venkateswara Institute of Medical Sciences, Tirupati, India, [4]Department of Mechanical Engineering, Northwestern University, Evanston, IL, United States

The need to understand how infection spreads to the deep lung was acutely realized during the severe acute respiratory syndrome coronavirus-2 (SARS-CoV-2) pandemic. The challenge of modeling virus laden aerosol transport and deposition in the airways, coupled with mucus clearance, and infection kinetics, became evident. This perspective provides a consolidated view of coupled one-dimensional physics-based mathematical models to probe multifaceted aspects of lung physiology. Successes of 1D trumpet models in providing mechanistic insights into lung function and optimalities are reviewed while identifying limitations and future directions. Key non-dimensional numbers defining lung function are reported. The need to quantitatively map various pathologies on a physics-based parameter space of non-dimensional numbers (a virtual disease landscape) is noted with an eye on translating modeling to clinical practice. This could aid in disease diagnosis, get mechanistic insights into pathologies, and determine patient specific treatment plan. 1D modeling could, thus, be an important tool in developing novel measurement and analysis platforms that could be deployed at point-of-care.

KEYWORDS

gas exchange, mucus balance, infection dynamics, trumpet model, aerosol transport and deposition, particle transport and deposition

1 Introduction

Deep lung infections had occurred commonly during the severe acute respiratory syndrome coronavirus-2 (SARS-CoV-2) pandemic causing unprecedented number of deaths (Wiersinga et al., 2020). One critical question was why this virus was infecting the deep lung much more than other respiratory viruses? How was the virus reaching into the deep lung so efficiently? Was it through the blood or the mucus lining or through aerosol transport in airways or was it growing due to favorable infection kinetics (Hagman et al., 2020; Tan et al., 2020; Edwards et al., 2021; Basu et al., 2022; Chakravarty et al., 2022; Chen et al., 2022; Darquenne et al., 2022a)? Direct experimental evidence of the underlying mechanism was difficult due to anatomical complexities of the lung as well as limitations of current measurement techniques. The need to rely on indirect evidence together with physical models was, thus, evident (Basu et al., 2022; Chakravarty et al., 2022; Chen et al., 2022; Darquenne et al., 2022a). Lung function is multifaceted and the challenge of modeling virus-laden aerosol transport and

deposition in the airways, *coupled with* mucus clearance and infection kinetics, became obvious (Chakravarty et al., 2022). This perspective reviews and consolidates various one-dimensional mathematical frameworks that can be a powerful tool to achieve this goal in the future.

One dimensional (1D) physics-based models have been providing useful mechanistic insights into lung function and optimalities (Taulbee and Yu, 1975; Darquenne and Paiva, 1994; Darquenne et al., 2022a). By 1D models, we imply that for each airway the physical variables are functions of the axial coordinate, while the radial and circumferential variations are averaged. We provide a unified view of the coupled physics to probe the multifaceted aspects of lung physiology. We interpret the results in a new light. For example, we highlight how steady-state solutions during inhalation are a limiting solution for gas invasion into the lung that can provide key insights into lung function. We provide an analytic steady-state solution for the first time and provide scaling arguments to guide our intuition about lung physiology. We show results based on known 1D models in literature to highlight the insights based on the effect of various non-dimensional numbers; understanding lung function via non-dimensional numbers is a perspective we emphasize in this article. We discuss how these calculations can be used to gain clinically relevant information for efficient drug delivery via lung or to understand deep lung infection (such as in SARS-CoV-2).

We tabulate the non-dimensional numbers defining lung function and discuss how it could provide a potential pathway to clinical translation. For example, we note an approach to measure and map various pathologies on a physics-based parameter space of non-dimensional numbers. Finally, this article supports the view that 1D modeling could be an important tool in developing novel platforms that can be deployed at point-of-care and that the physics community can contribute toward that vision.

1.1 Background of lung physiology and modeling

The respiratory system is one of the most exposed organ systems of the human body (West, 2012). It has a complex anatomy which can be broadly subdivided into two regions - the *upper respiratory tract* (URT) and the *lower respiratory tract* (LRT). The URT comprises the nose, paranasal sinuses, mouth, nasal cavity, pharynx and larynx. The LRT can be further demarcated into the *tracheobronchial tree* and the *alveolar region*. The tracheobronchial tree (also called upper or conducting airways) comprises the trachea and the dichotomous bifurcating bronchial structure (see Figures 1a,b), exhibiting self-similar fractal properties. The alveolar region consists of the terminal airways and the alveoli. The bronchial network, along with the alveolar region, is commonly referred to as the *lung*. The alveolar region is sometimes also termed the *deep lung* due to its terminal location (West, 2012; Weibel et al., 1963). Pertinent information on lung anatomy is summarized in Table 1.

The large surface area of the lung enables easier respiration through a mechanism which draws in ambient air during inhalation and releases expired air during exhalation. However, it also makes the pulmonary system (and in turn, other internal organs of the body) vulnerable to health hazards from polluting particles and infected droplets, among others, which may enter the respiratory tract during inhalation along with the ambient air. Air, along with suspended particles and droplets, is inhaled into the respiratory tract through the URT, which are transported deeper into the LRT through the conducting airways to reach the deep lung (Pedley, 1977). Gas exchange with the blood stream takes place in the deep lung. The reverse happens during exhalation. While some of the inhaled particles/droplets may get exhaled out, a considerable fraction of these may get deposited in the airway and alveoli as a result of various forces acting on them (Hofmann, 2011). Their deposition takes place in the respiratory mucosa - a thin layer of mucosal fluid that separates the airway lumen from the epithelial tissue (Mauroy et al., 2011; Karamaoun et al., 2018; Chakravarty et al., 2022). The thickness of the mucosal layer is $\mathcal{O}(50)$ μm in the trachea and reduces as one moves deeper becoming negligible in the terminal airways (Mauroy et al., 2011). The mucosal fluid is also subjected to periodic ciliary beating which results in advective transport of the fluid towards the trachea. The deposited particles/droplets are, as such, transported along with the mucosal fluid, in addition to diffusion, resulting in a self-clearance mechanism (Mauroy et al., 2011) Pulmonary drug delivery systems also rely on this mechanism to deliver aerosolised medicinal drugs to the lung in a non-invasive manner (He et al., 2022).

A large body of literature exists detailing the extensive investigations that have been carried out on gas exchange dynamics as well as particle/droplet transport and deposition within the respiratory tract (Pedley, 1977; Hofmann, 2011; Guha, 2008; Kleinstreuer and Zhang, 2010). Nonetheless, certain aspects - such as the dynamics of viral respiratory infections - still require further investigations (Neelakantan et al., 2022). Infected virus-laden droplets are the main source for transmission of viral respiratory infections such as SARS-CoV-2 (Wiersinga et al., 2020; Harrison et al., 2020; Mittal et al., 2020; Wang et al., 2021; Leung, 2021). These droplets are formed within the respiratory tract of an infected individual (Abkarian et al., 2020; Darquenne et al., 2022a; Morawska et al., 2022) and are subsequently exhaled out during breathing, coughing, sneezing, talking, etc. This leads to formation of turbulent clouds of air containing suspended virus-loaded droplets (Bourouiba, 2021). These droplets may be inhaled by other individuals causing the inhaled droplets to deposit in the respiratory mucosa releasing the entrained viruses and starting an infection in the new subject (Wiersinga et al., 2020; Grant et al., 2021). A complete spectrum of respiratory virus transmission, thus, includes the following components: a) droplet formation from infected respiratory mucosa inside the respiratory tract, b) external transmission of infected droplets through respiratory motions and the effect of preventive measures (such as masks) on such transmission, and c) internal transmission of the inhaled infected droplets within the respiratory tract. A thorough understanding of all of these components is, as such, required in order to fully comprehend the fluid dynamics of respiratory virus transmission.

Extensive studies have been carried out on external transmission of droplets (Abkarian and Stone, 2020; Bourouiba, 2021), especially since the beginning of the SARS-CoV-2 pandemic. These studies have analysed different physical settings with respect to transmission mechanisms, environmental factors, and physical configurations with a focus on identifying the risk of infection spread and possible preventive measures (Pal et al., 2023; Biswas et al., 2022).

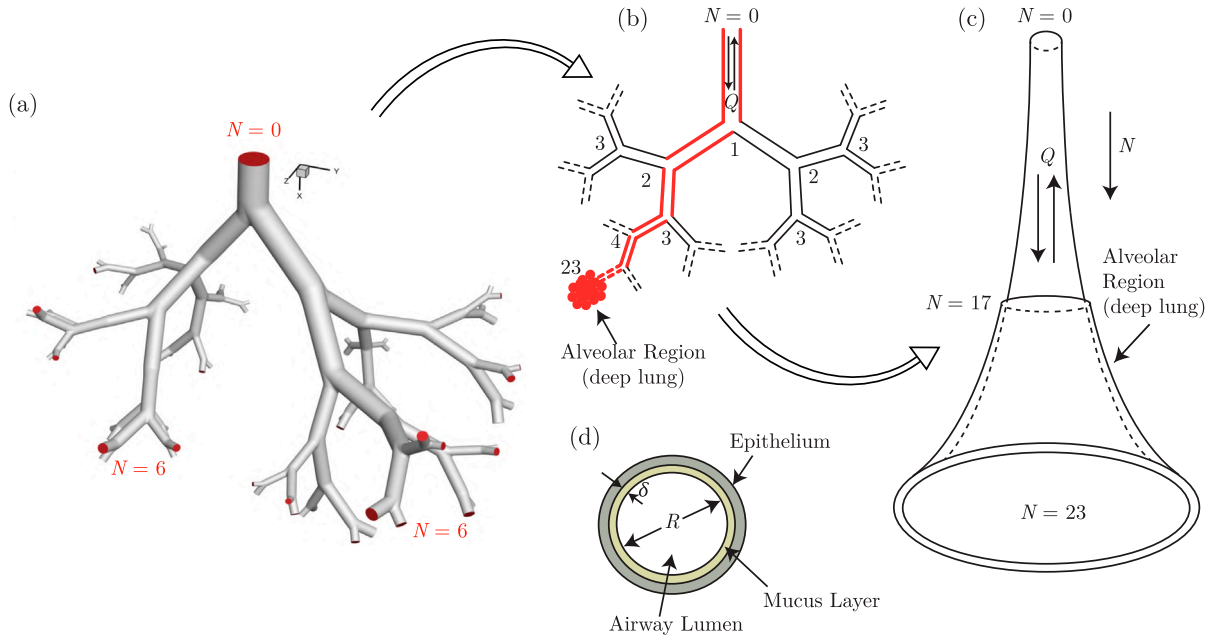

FIGURE 1
Illustration of the development of the *trumpet* model from an anatomical dichotomous branching network of the lower respiratory tract (LRT). **(a)** A typical branching network of the LRT is shown in the form of a model geometry up to the sixth generation (Ghorui et al., 2024) and the corresponding schematic representation is shown in **(b)** The red colored pathway highlights a single continuous link of the airway network connecting the extremities. The single continuous link, when lumped considering all branches of each generation, results in a single continuous channel of variable cross-sectional area. This is referred to as the *trumpet* model **(c)** The respiratory mucus lining the respiratory tract, as considered in the *trumpet* model, is shown in **(d)** Parts of this figure are reproduced with permission from (Ghorui et al., 2024; Chakravarty et al., 2022; Chakravarty et al., 2023).

TABLE 1 Anatomical parameters for representative lung generations Yeh and Schum (1980).

N	N_a	D (cm)	L (cm)	θ (°)	ϕ (°)	$\sum S$ (cm^2)	$\sum V$ (cm^3)
0	1	2.01	10.0	0	0	3.17	31.73
1	2	1.56	4.36	33	20	3.82	48.4
2	4	1.13	1.78	34	31	4.01	55.54
3	8	0.827	0.965	22	43	4.3	59.69
4	16	0.651	0.995	20	39	5.33	64.98
10	1,024	0.198	0.556	33	43	31.53	148.59
15	32,768	0.06	0.168	51	60	150.09	247.32
20	1,048,576	0.044	0.07	45	60	1,594.39	498.36
23	8,388,608	0.043	0.053	45	60	12,181.95	1,692.08
**	-	-	-	-	-	-	5563.88

N, Lung Generation; N_a, Number of airways in a generation; D, Airway diameter; L, Airway length; θ, Branching angle: ϕ, Gravity angle; S, Total cross-sectional area in a generation; V, Total volume in a generation; *: Alveoli.

While there has been evidence of increased number of aerosols exhaled during SARS-CoV-2 infection (Edwards et al., 2021), relatively fewer studies have dealt with droplet formation from respiratory mucosa inside the respiratory tract (Hamed et al., 2020; Pairetti et al., 2021; Anzai et al., 2022; Haslbeck et al., 2010; Kant et al., 2023; Morawska et al., 2022; Saha et al., 2024). These droplets, once formed, may then be exhaled out or internally transmitted within the respiratory tract (Chakravarty et al., 2023; Anzai et al., 2022). Understanding the mechanism of formation of these droplets from respiratory mucosa is critical to identifying

the conditions which aid droplet formation and hence, increase the risk of infection transmission - externally as well as internally. Internal transmission of infected droplets within the respiratory tract is also hypothesized to be a plausible mechanism by which a viral infection may spread to the inner regions of the respiratory tract, including the alveolar region (deep lung), where it may cause serious diseases such as pneumonia, acute respiratory distress syndrome etc. (Grant et al., 2021).

As discussed previously, many studies have been carried out on internal droplet transmission and deposition in the respiratory tract. These include analytical, computational as well as limited experimental studies (*in vivo*, *in vitro* as well as *ex vitro*) (Morawska et al., 2022). However, there are not many studies that have taken into account mucosal flow dynamics coupled with pathogen-specific effects, along with internal droplet transmission, while distinguishing between various types of infections and their spread (Quirouette et al., 2020). While discrete studies (experimental as well as computational) on mucus dynamics and infection kinetics are available (Baccam et al., 2006; Mauroy et al., 2011; Banerji et al., 2023; Looney et al., 2011; Ravi et al., 2025), the coupled effects need to be investigated to fully characterize the underlying phenomena. Experimental investigations of such coupled phenomena is prohibitively difficult due to various reasons (Morawska et al., 2022) necessitating reliance on computational studies. This perspective focuses specifically on this aspect–fluid dynamics of internal droplet transmission within the respiratory tract in addition to gas exchange, coupled with mucus flow dynamics and pathogen-specific effects. One dimensional (1D) models are surveyed due to their ease of use and efficacy in providing useful clinically relevant mechanistic insights.

Different computational techniques have been used in the past to model droplet transport and deposition in the respiratory tract (Hofmann, 2011; Guha, 2008; Koullapis et al., 2019; Neelakantan et al., 2022). Geometrical complexity of the respiratory tract, however, makes it difficult (if not impossible) to carry out high-resolution computational analyses considering the complete lung geometry. High-resolution investigations have, therefore, been carried out separately targeting specific truncated regions of the respiratory tract - the upper bronchial region (Koullapis et al, 2016; Basu, 2021), the central conducting airways (Koullapis et al., 2018b; Ghorui et al., 2024) or the terminal alveolar region (Chakravarty et al, 2019; Sznitman, 2013; Fishler et al., 2015) - with appropriate boundary conditions. Some studies have also considered combinations of these regions in their analyses by employing different coupling techniques (Koullapis et al., 2018a; Koullapis et al., 2020; Kuprat et al., 2021; Koullapis et al., 2023). Several studies have also been carried out on droplet transport and deposition in the URT (Basu et al., 2020; Basu, 2021). These studies are useful in modelling geometrical complexities of the respiratory tract (often using high-resolution data obtained from computed-tomography scans (Tawhai et al., 2004)) and provide useful information regarding the local fluid dynamics as well as insights into the mechanism of droplet deposition in the modelled region (Basu et al., 2020; Basu, 2021). Detailed information of droplet transport and deposition for the complete respiratory tract is expensive and difficult using this approach, although some advances has been made in this direction recently through development of computed tomography-based whole lung deposition models (Zhang et al., 2022) and use of self-similar bifurcating units, based on lung fractal geometry Ghorui et al. (2024). Simplified models of the respiratory tract are, therefore, useful when the goal is to capture the key trends of droplet transport and deposition for the complete respiratory tract. In this context, *one-path* lung models–which considers a single, representative airway path from the trachea to the alveoli–have been utilised. This concept originates from the "Typical Path Lung Model" introduced by Yeh and Schum (1980). Similar one-path models of the lung have been recently utilized for extensively studying flow perturbations through direct numerical simulations (Atzori et al., 2025) as well as for investigation of aerosol flow and deposition through experiments (Möller et al., 2021).

A different class of simplified models are based on morphometry of the respiratory tract (Weibel et al., 1963; Raabe, 1976) and can be broadly classified into semi-empirical regional *compartment* models and one-dimensional *trumpet* models (Hofmann, 2011). While these simplified models cannot account for the effects of heterogeneity in the lung, these are extremely useful for understanding the fundamental mechanisms and capturing key trends of aerosol transport and deposition for the whole lung. The *compartment* models assume that the lung morphology is comprised of four different compartments - extrathoracic, bronchial, bronchiolar, and alveolar regions (Hofmann, 2011; Neelakantan et al., 2022) Separate mathematical models have been developed for each of these compartments, based on analogy with an equivalent electrical circuit, in order to obtain the gas transport and exchange characteristics (Nunn, 1957; Ben-Tal, 2006). Different semi-empirical models are utilised, along with the gas transport models, for determining the deposition of inhaled aerosols within the compartments (Hofmann, 2011) This technique provides an estimate of the compartment-wise deposition of aerosols.

The *trumpet* model, on the other hand, is a 1D approximation of the anatomical dichotomous branching network of the complete respiratory tract (Paiva, 1973; Darquenne and Paiva, 1994; Choi and Kim, 2007; Devi et al., 2016; Chakravarty et al., 2022; 2023). This technique considers the respiratory tract to be a continuous channel of variable cross-sectional area (see Figure 1c). The length and cross-sectional area of the approximated channel are determined using different empirical correlations based on airway generation number (N) and other anatomical parameters. The present work uses a *trumpet* model where the number of branches (N_l), length (L) and the total cross-sectional area (A) at each generation (N) is calculated using a power-law function as (Chakravarty et al., 2022; Chakravarty et al., 2023)

$$N_l = 2^N, L(N) = L_0\alpha^N, A(N) = A_0(2\beta)^N, \tag{1}$$

where L_0 and A_0 are the length and cross-sectional area at $N = 0$ (trachea), respectively. α and β are the length-change and area-change factors selected such that the computed length and area at each generation closely matches Weibel's morphometric data (Weibel et al., 1963) (see Figure 2a). Alveolation of the distal lung airways is considered $N = 17$ onwards, consistent with human lung (Weibel et al., 1963), by considering additional surface area in the relevant generations (Chakravarty et al., 2022; 2023). The modeled system of airways and alveoli is also assumed to be lined by a thin mucus layer separating the airway lumen from the underlying periciliary layer and the epithelium (see Figure 1d).

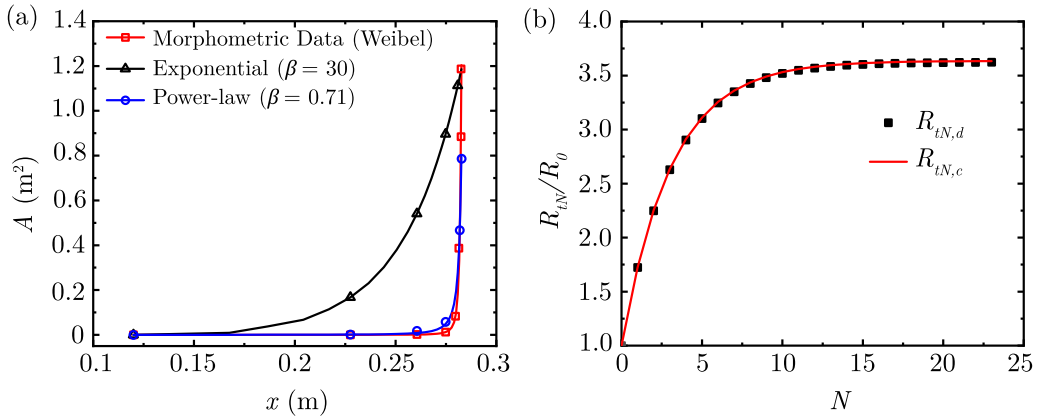

FIGURE 2
(a) Comparison of area variation in the lung along its length considering the exponential and power-law models with the morphometric data of Weibel (Weibel et al., 1963) **(b)** Comparison of airway resistance to airflow (R_{tN}/R_0) determined using the discrete (Equation 9) and continuous solutions (Equation 12) considering $\alpha = 0.73, \beta = 0.71$.

The periciliary layer, the epithelium and the ciliary motion driving mucus transport are not explicitly modelled. Instead, mucociliary transport is accounted for by assuming a convective motion in the mucus layer from the deeper generations (larger N) towards $N = 0$. The thickness (δ), the total cross-sectional area of the mucus layer (A_m), and the convective mucus velocity (V_m) at different airway generations are also estimated using power law functions as (Chakravarty et al., 2022; Chakravarty et al., 2023)

$$\delta(N) = \delta_0 \zeta^N, A_m(N) = A_{m,0}\left(2\sqrt{\beta}\zeta\right)^N, V_m(N) = V_{m,0}\varepsilon^N, \text{for N} < 18,$$
$$= 0, \text{for N} \geq 18, \tag{2}$$

where δ_0, $A_{m,0}$, and $V_{m,0}$ are the mucus thickness, area, and velocity at $N = 0$, respectively. The magnitudes of the change factors ζ and ε are chosen based on reported data (Karamaoun et al., 2018; Foster et al., 1980; Yeates et al., 1975). V_m is assumed to be zero beyond $N = 17$ (Equation 2) due to the absence of appreciable mucociliary transport in the deep lung (Mauroy et al., 2011). δ and V_m are also assumed to be temporally invariant in this analysis (Karamaoun et al., 2018). The reasoning for this assumption is discussed in detail in Section 3.

This perspective starts with airway fluid dynamics based on 1D assumptions. It is followed by the transport equations for gas exchange, particle/droplet transport, deposition and clearance and finally, pathogen-specific effects. The goal is to consolidate key insights obtainable from 1D models because of which it has remained a useful model to draw mechanistic insights into lung physiology.

2 Airway fluid dynamics

2.1 Airflow

In order to develop the airflow transport equations, it is necessary to *a priori* examine the nature of airflow within the lung and make reasonable assumptions. Scaling based on relevant physiological parameters shows that Reynolds number (Re) varies between $10^3 - 6 \times 10^{-3}$ within the lung. Re reduces from about 10^3 at $N = 0$ (trachea) to less than 10 after $N = 13$ (airways) and to less than 1 after $N = 17$ (deep lung), as established through various studies including microfluidic experiments (Pedley, 1977; Kleinstreuer and Zhang, 2010; Sznitman, 2021; Kassinos and Sznitman, 2025). This implies that airflow within most of the lung remains largely laminar. Neglecting turbulence is, thus, a reasonable assumption in most of the lung. Nonetheless, localised air circulation zones can still form near airway bifurcations and in the deep lung which can impact particle/aerosol deposition (Kassinos and Sznitman, 2025).

The pulsatile nature of breathing introduces unsteadiness to airflow in the upper airways. This allows the use of the Womersley number (Wo), which originates from a solution of the linearised Navier-Stokes' equation for oscillatory laminar flow in an infinitely long pipe and subseuquently applied to characterization of pulsatile blood flow in an arterial tree, in quantifying the unsteady effects of airflow (Pradhan and Guha, 2019; Chakravarty et al., 2019; Sznitman, 2021). Wo is defined as the ratio of inertial to viscous forces in a pulsatile flow i.e., $Wo = D\sqrt{\omega/\nu}$, where D, ω and ν denote the airway diameter (see Table 1), pulsatile frequency and kinematic viscosity of air, respectively. Thus, if $Wo > 1$, inertial forces dominate resulting in significant unsteady effects. On the other hand, if $Wo < 1$, the viscous forces dominate resulting in the flow-field developing fully during each pulsation cycle. The latter allows a quasi-steady approximation. Analysis of airflow in the airways show that Wo ranges between $6 - 0.1$, with $Wo < 2$ for $N > 2$. This implies that the unsteady pulsatile flow effects exist only in the first couple of generations beyond which the flow remains largely quasi-steady (Sznitman, 2021). A quasi-steady assumption in modelling lung airflow is, thus, a reasonable approximation.

The 1D transport equations for airflow dynamics are summarized next and the corresponding analysis is presented using the above approximations (also detailed in the subsequent sections). It is to be noted that while the balance equations for mass and momentum are fundamental to modeling lung airflow

dynamics, the corresponding energy and entropy balances are typically not invoked. This is because temperature variations during normal respiration are small, viscous dissipation is negligible, and thermal nonequilibrium effects are minimal Pedley (1977), West (2012), Karamaoun et al. (2018) In addition, while some degree of phase change exists in the first few generations Karamaoun et al. (2018), it's effect on airflow and particle deposition is not significant. Consequently, energy and entropy transport do not exert a meaningful influence on airflow or particle deposition.

2.1.1 1D unsteady airflow

The 1D transport equation for airflow in the idealized lung geometry can be expressed using Equations 3, 4 as

Mass transport:

$$\frac{\partial(\rho A_x)}{\partial t}+\frac{\partial(\rho Q)}{\partial x}=0, \tag{3}$$

Momentum transport:

$$\rho\frac{\partial}{\partial t}\left(\frac{Q}{A_x}\right)+\rho\frac{\partial}{\partial x}\left(\frac{1}{2}\left(\frac{Q}{A_x}\right)^2\right)=-\frac{\partial p}{\partial x}-\frac{8\pi\mu\beta_c Q}{N_l A_l^2}, \tag{4}$$

where ρ, μ, Q and p are the air density, air viscosity, volume flow rate of air, and pressure, respectively. A_x is the total cross-sectional area of the airway at a particular position (x) defined such that it increases as one goes farther from the trachea (see Figure 1). N_l is the number of branches in each airway generation (see Equation 1). The last term on the right hand side of the momentum transport equation (Equation 4) takes into account the viscous flow resistance and is similar to that obtained in Hagen-Poisseuille flow with a constant cross-sectional area. β_c takes into account the unsteady effects of pulsatile flow and can be determined after averaging the Womersley solution. Note that $\beta_c = 1$ for a parabolic velocity profile (Hagen-Poisseuille flow).

2.1.2 1D steady state airflow

As noted earlier, the quasi-steady laminar nature of airflow through the lung also makes it possible to neglect the inertia terms in Equation 4 resulting in

$$\frac{\partial p}{\partial x}=-\frac{8\pi\mu\beta_c Q}{N_l A_l^2}. \tag{5}$$

Thus, the airflow in the lung is largely determined by a balance between the pressure gradient and the viscous resistance. This simplification makes it possible to estimate the resistance to airflow in the entire lung. Assuming that the lung has a symmetric branching structure (see Figure 1), then there are 2^N parallel branches at each generation (N). It is also assumed that all branches in a single generation are identical. Resistance of a single branch of the N^{th} generation (R_{1N}) for such a symmetric lung geometry can be determined using Equation 5 as

$$R_{1N}=\frac{\Delta p}{Q}=\frac{8\pi\mu\beta_c L_N}{A_l^2}. \tag{6}$$

Since. airflow through the branches is similar to flow through parallel channels (Popel, 1980; Soni et al., 2020), the total resistance for the N^{th} generation (R_N) can be determined using Equation 6 to be

$$R_N=\frac{8\pi\mu\beta_c L_N}{N_l A_l^2}. \tag{7}$$

Using Equation 1, this can be further reduced to

$$R_N=\left(\frac{8\pi\mu\beta_c L_0}{A_0^2}\right)\left(\frac{\alpha}{2\beta^2}\right)^N=R_0\left(\frac{\alpha}{2\beta^2}\right)^N, \tag{8}$$

where, $R_0\left(=\frac{8\pi\mu\beta_c L_0}{A_0^2}\right)$ is the resistance in $N = 0$. Using Equation 8, the total resistance up to the end of the N^{th} generation ($R_{tN,d}$) can be determined by adding resistances in series, following geometric progression, as

$$\begin{aligned}R_{tN,d}&=R_0+R_0\left(\frac{\alpha}{2\beta^2}\right)+R_0\left(\frac{\alpha}{2\beta^2}\right)^2+\cdots.+R_0\left(\frac{\alpha}{2\beta^2}\right)^N\\&=R_0\frac{\left[1-\left(\frac{\alpha}{2\beta^2}\right)^{N+1}\right]}{\left[1-\left(\frac{\alpha}{2\beta^2}\right)\right]}.\end{aligned} \tag{9}$$

Alternatively, the total airway resistance can also be determined by integrating the resistance per unit length over the entire length of the airway. Using Equation 1, the total airway length up to the N^{th} generation can be determined to be

$$x_N=L_0+L_0\alpha+L_0\alpha^2+\cdots+L_0\alpha^N=L_0\frac{\left(1-\alpha^{N+1}\right)}{(1-\alpha)}, \tag{10}$$

which gives us

$$dx_N=-L_0\frac{\alpha\ln\alpha}{(1-\alpha)}\alpha^N dN. \tag{11}$$

Using Equations 7, 10, 11, the total airway resistance up to the end of the N^{th} generation ($R_{tN,c}$) can be determined as

$$\begin{aligned}R_{tN,c}&=R_0+\int_{x_0}^{x_N}\frac{8\pi\mu\beta_c}{N_l A_l^2}dx=R_0+\int_0^N\left[-R_0\frac{\alpha\ln\alpha}{(1-\alpha)}\left(\frac{\alpha}{2\beta^2}\right)^N\right]dN\\&=R_0\left[1+\left(\frac{\alpha\ln\alpha}{(1-\alpha)\ln\left(\frac{\alpha}{2\beta^2}\right)}\left[1-\left(\frac{\alpha}{2\beta^2}\right)^N\right]\right)\right],\end{aligned} \tag{12}$$

where x_0 ($= L_0$) is the length of the 0^{th} generation ($N = 0$).

The two solutions obtained by Equations 9, 12 are compared in Figure 2b for physiologically relevant values of α and β (see Equation 1). The two solutions are in excellent agreement, which allows either solution to be utilised for analysis. It is noted that major deviations of β from physiologically relevant values will cause the two solutions to diverge from each other. The technique used in obtaining Equation 12 will be used to develop and solve other transport equations discussed subsequently in this article. It will be found to be useful to get analytic solutions and obtain useful insights into gas transport in the lung.

2.2 Gas exchange

Along with airflow dynamics, it is essential to study the mechanism of transport and exchange of various constituent gases (of air) in the lung since breathing induces spatio-temporal variations in gas concentration within the lung (Hasler et al., 2019;

Tsuda et al., 2008). The 1D transport equation for gases in the idealized lung geometry (see Figure 1) is expressed as

$$\frac{\partial\left(\rho A_x c_g\right)}{\partial t}+\frac{\partial\left(\rho Q c_g\right)}{\partial x}=\frac{\partial}{\partial x}\left(\rho A_x D_g\frac{\partial c_g}{\partial x}\right)-\left(\rho L_{ex}\left(c_g-c_\infty\right)\right),\quad(13)$$

where c_g, Q, and D_g are the gas concentration (in air), volume flow rate of air during breathing, and gas diffusivity (in air), respectively. ρ is the gas density and A_x is the cross-sectional area of the lung at a particular location x. The last term on the right hand side of Equation 13 takes into account gas exchange with the blood stream (having a gas concentration $c_{g,\infty}$). L_{ex} is defined as the loss coefficient due to gas exchange with the blood stream and is expressed as

$$L_{ex}=2\pi R D_{ex},\quad(14)$$

where $R\left(=R_N 2^N\right)$ is the total perimeter in the N^{th} generation and D_{ex} is the rate at which the gas is exchanged with the blood stream. Since gas exchange occurs only in the alveolar region of the lung (Tsuda et al., 2008; West, 2012), the loss term (Equation 14) is also considered only in the alveolar region of the idealized lung geometry and neglected in the upper airways. Here alveolar capacitance (or lung elasticity) effects could be modeled but are not explicitly elaborated here (Neelakantan et al., 2022).

Steady and unsteady solutions to Equation 13 are provided in Sections 2.2.1, 2.2.2, respectively. Fluid motion and hence, gas transport during breathing is inherently unsteady with a time-periodic nature (Chakravarty et al., 2019) - it takes more than 10 breathing cycles (normal breathing cycle ~4s) for gas concentration to reach a time-periodic state. This warrants unsteady analysis. However, the steady-state solution provides useful insights into the transport mechanism and the governing parameters, and it can be used to identify the limiting solution for different flow conditions.

2.2.1 1D steady-state gas exchange: a reference solution

The following assumptions are made while solving Equation 13 using the steady-state approach: a) all parameters are time-invariant, b) airflow within the lung geometry remains uniform and unidirectional, c) gas concentration at the entrance to the trachea ($N=0$) remains constant, and d) total alveolar gas exchange occurs at the last generation of the lung ($N=23$).

Considering these assumptions, Equation 13 simplifies to

$$\frac{\partial}{\partial x}\left[\left(Qc_{g,x}\right)-\left(A_x D_g\frac{\partial c_{g,x}}{\partial x}\right)\right]=0,\quad(15)$$

which is solved analytically for two scenarios and numerically for a particular case. The analytic solutions are discussed first, followed by the numerical solution.

2.2.1.1 1D analytical solution: exponential variation

The total cross-sectional area (A_x) along the length of the idealised lung geometry may be approximated using an exponential function as

$$A_x=A_0\exp\left(\beta x\right),\quad(16)$$

where A_0 is the cross-sectional area at $x=0$ and β is the area-change factor (see Section 1; Figure 2a). The analytical solution of gas concentration obtained considering this approximation (Equation 16) is expressed as

$$\lim_{c_{g,\infty}\to 0}\frac{c_{g,x}}{c_{g,0}}=\phi_{g,x}=1+\frac{\left[\exp\left[Pe_{g,e}\left(1-e^{-\beta L}\right)\right]-\exp\left[Pe_{g,e}\left(e^{-\beta x}-e^{-\beta L}\right)\right]\right]\left[1-\frac{Z}{e^{-\beta L}}\right]}{1-\left[\exp\left[Pe_{g,e}\left(1-e^{-\beta L}\right)\right]\left[1-\frac{Z}{e^{-\beta L}}\right]\right]},\quad(17)$$

where $Pe_{g,e}\left(=\frac{QL_0}{A_0 D_g}\right)$ and $Z\left(=\frac{Q}{A_0 D_{ex}}\right)$ represents the Peclet number for gases (exponential variation) and the gas exchange parameter with the blood stream, respectively. A detailed derivation of the analytical solution and definition of various terms can be found in (Supplementary Section S1).

The magnitude of $Pe_{g,e}$ of interest in respiratory gas transport ranges from $1000-64500$ based on gas diffusivity in air and air flow rates in breathing. This makes it intractable to determine the magnitude of $\exp\left[Pe_{g,e}\left(1-e^{-\beta L}\right)\right]$ in Equation 17. However, it can be used for smaller $Pe_{g,e}$. Additionally, we note that there is a large quantitative difference between the area obtained using the exponential function and the morphometric data (see Figure 2a; the magnitude at the alveolar end of the lung remains in good agreement). Therefore, the exponential function is not the best fit to the area variation in the lung. However, it models the physics of gas transport in a rapidly diverging duct, which is similar to the lung.

2.2.1.2 1D analytical solution: power-law variation

An alternate approach for a better fit is to approximate the length (L_N) and the total cross-sectional area (A_N) at each generation (N) of the idealised lung geometry using a power-law function (see Section 1; Figure 2a; Equation 1). The length-change (α) and area-change (β) factors in Equation 1 are selected such that the computed length and area at each generation matches Weibel's morphometric data Weibel et al. (1963) as closely as possible (see Figure 2a). The airway length (x), in terms of the lung generation number (N), is given by

$$x_N=\frac{L_0\left(1-\alpha^{N+1}\right)}{1-\alpha}.\quad(18)$$

Since the length and area variation is assumed to be a function of N (see Equations 1, 18), the steady-state gas transport equation (Equation 15) is re-written in terms N as

$$\frac{\partial}{\partial N}\left(Qc_{g,N}-A_N D_g H_N\frac{\partial c_{g,N}}{\partial N}\right)=0,\quad(19)$$

using $H_N=\frac{\partial N}{\partial x_N}$. It is to be noted that although N is an integer, it is treated as a continuous variable in all transport equations for computational convenience. The analytic solution of Equation 19 for gas concentration following this approach is given by

$$\lim_{c_{g,\infty}\to 0}\frac{c_{g,N}}{c_{g,0}}=\phi_{g,N}=1+\frac{\left[\exp\left[Pe_{g,pl}\left(\delta^N-1\right)\right]-\exp\left[Pe_{g,pl}\left(\delta^M-\delta^N\right)\right]\right]\left[1-\frac{Z}{2\beta^M}\right]}{1-\left[\exp\left[Pe_{g,pl}\left(\delta^M-1\right)\right]\right]+\left[Z\frac{\exp\left(Pe_{g,pl}\left(\delta^M-1\right)\right)}{(2\beta)^M}\right]},\quad(20)$$

where, $Pe_{g,pl}\left(=\frac{QL_0\alpha\ln(\alpha)}{A_0 D_g(1-\alpha)\ln(\alpha/2\beta)}\right)$ represents the Peclet number for gases (power-law variation) and $Z\left(=\frac{Q}{A_0 D_{ex}}\right)$ is the gas exchange parameter with the blood stream, respectively. Detailed derivation

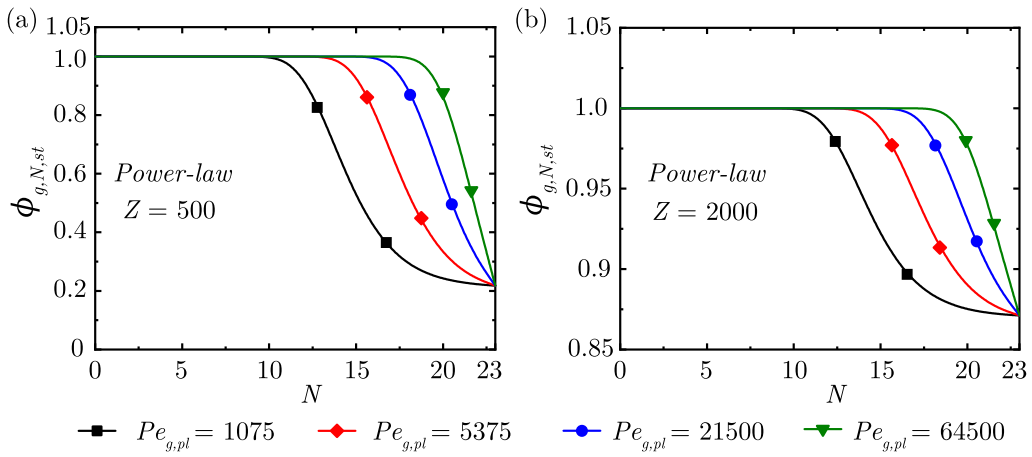

FIGURE 3
Change in steady-state dimensionless gas concentration ($\phi_{g,N,st}$) within the lung for different $Pe_{g,pl}$ at **(a)** Z = 500 and **(b)** Z = 2,000 considering α = 0.73, β = 0.71. Note the change in scales between the two figures.

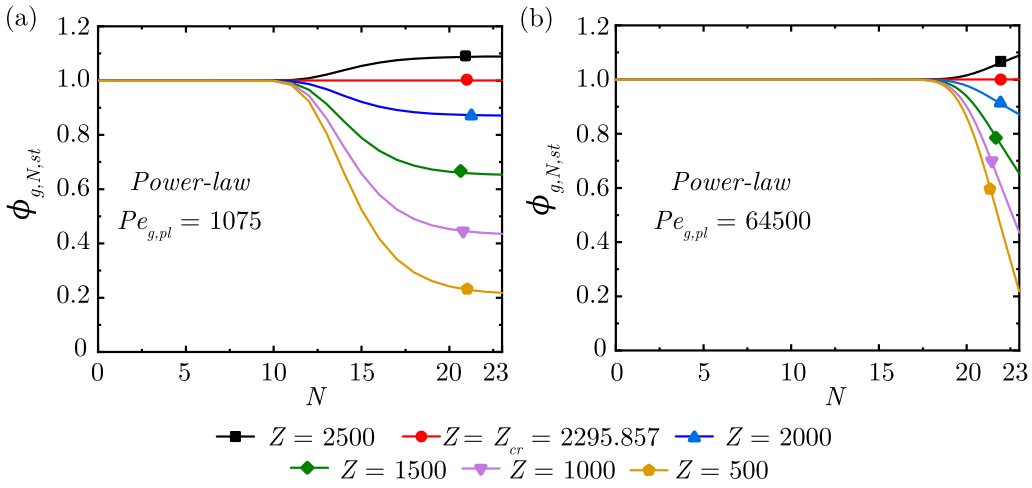

FIGURE 4
Change in steady-state dimensionless gas concentration ($\phi_{g,N,st}$) within the lung for different magnitudes of the gas exchange parameter (Z) at **(a)** $Pe_{g,pl}$ = 1,075 and **(b)** $Pe_{g,pl}$ = 64,500 considering α = 0.73, β = 0.71. Note the change in $\phi_{g,N,st}$ in the Deeper lung generations (larger N) based on the critical magnitude of Z (Z_{cr}).

of the analytical solution and definition of various terms can be found in (Supplementary Section S2). It is to be noted that Equation 20 also contains terms of the form $\exp\left(Pe_{g,pl}(\delta^N - 1)\right)$ (similar to Equation 17). However, this form is tractable since the small magnitudes of δ^N negates the large magnitude of $Pe_{g,pl}$ and allows calculation of $c_{g,N}$.

The major governing parameters in Equation 20 are the Peclet number for gases ($Pe_{g,pl}$) and the gas exchange parameter (Z), respectively. Figures 3, 4 compares the steady-state $\phi_{g,N}$ for different $Pe_{g,pl}$ (~1000 – 64500) and Z (~500 – 2500). The range of $Pe_{g,pl}$ considered corresponds to physiological flow rates and gas diffusivity in air. The range of Z is determined by varying the exchange rate (D_{ex}).

It is observed from Figure 3 that, as expected, the gas concentration front propagates deeper into the lung with increase in $Pe_{g,pl}$ for all magnitudes of Z. The concentration front demarcates the region where diffusive transport dominates from the region where convective transport dominates. For a given gas diffusivity, a larger $Pe_{g,pl}$ results in a greater impact of convection over diffusion and vice-versa. Greater convective transport causes the gas to reach deeper into the lung and hence, the concentration front also propagates towards the deep lung with increase in $Pe_{g,pl}$.

The impact of Z on the gas exchange process is shown in Figure 4. A larger Z indicates a smaller gas exchange rate and consequently, a greater $\phi_{g,N}$ at N = 23. A critical magnitude (Z_{cr} = 2295.857) is obtained when no gas exchange takes place with the blood stream and $\phi_{g,N}$ remains invariant throughout the lung. Any Z larger than this Z_{cr} results in gas accumulation within the lung. It is also evident from Figures 3, 4 that the location of the concentration front is determined by the combined effects of $Pe_{g,pl}$ and Z. The magnitude

of $\phi_{g,N}$ at $N = 23$ is, however, independent of $Pe_{g,pl}$ and is solely determined by Z.

2.2.1.3 1D numerical solution

The theoretical solutions discussed in the preceding sections considered steady-state transport of gases within the lung for unidirectional air flow. Physiologically, air flow and hence, transport of gases is unsteady and bi-directional with periodic flow reversals depending on the breathing frequency. A numerical method is necessary to obtain an unsteady solution of gas transport equation (Equation 13). The following scaling parameters (Equation 21) are used to reduce Equation 13 to an appropriate dimensionless form (Equation 22) using the power-law assumption (Equation 1).

$$\begin{aligned}\phi_{g,N} = \frac{c_{g,N}}{c_{g,0}}, \tau = \frac{t}{T_b}, Q = Q_{max} q(t), T_a = \frac{L_0 A_0}{|Q_{max}|}, St_a = \frac{T_a}{T_b},\\ Pe_g = \frac{|Q_{max}| L_0}{A_0 D_g} = Pe_{g,pl} \frac{(1-\alpha)\ln(\alpha/2\beta)}{\alpha \ln(\alpha)\, q(t)},\end{aligned} \tag{21}$$

where, Pe_g and St_a are the Peclet number for gases and Strouhal number for the airways, respectively. $\phi_{g,N}$ and τ denotes the dimensionless gas concentration and time, respectively, while the quantities T_a and T_b represents the convective airflow time-scale and breathing time-scale, respectively. The dimensionless equation used to numerically analyse gas transport within the lung is given by

$$\left[|Pe_g| St_a (2\alpha\beta)^N\right] \frac{\partial \phi_{g,N}}{\partial \tau} = \frac{\partial F_{g,N}}{\partial N} - \left(L'_{ex} \phi_{g,N}\right), \tag{22}$$

where

$$F_{g,N} = \left[\left(\left(\frac{2\beta}{\alpha}\right)^N \left(\frac{1-\alpha}{\alpha(\ln\alpha)}\right)^2 \frac{\partial \phi_{g,N}}{\partial N}\right) + \left(|Pe_g| q(t) \left(\frac{1-\alpha}{\alpha \ln(\alpha)}\right) \phi_{g,N}\right)\right], \tag{23}$$

$$L'_{ex} = L_{ex} \frac{L_0^2}{A_0 D_g} \alpha^N = \frac{|Pe_g| \alpha^N}{Z} \left(\frac{2\pi R L_0}{A_0}\right). \tag{24}$$

Equation 22, along with Equations 23, 24, can be solved numerically (Chakravarty et al., 2019; 2022).

Figure 5 shows the progression of $\phi_{g,N}$ with time advancement within the lung for unidirectional flow. It can be observed that $\phi_{g,N}$ reaches a steady-state within 5 breathing cycles ($\tau \sim 5$) and that the steady-state $\phi_{g,N}$ obtained using the numerical technique matches the theoretical prediction (Equation 20). Additional comparisons between numerical and theoretical predictions at steady-state are shown in Supplementary Figure S1 for the extreme magnitudes of $Pe_{g,pl}$ and Z considered in this study. It can be observed that the numerical solution is able to appropriately capture the trends in $\phi_{g,N}$ for the entire range of $Pe_{g,pl}$ and Z considered in this study for unidirectional flow at steady-state.

2.2.2 1D unsteady gas exchange

Physiologically realistic airflow in the lung is unsteady and bi-directional in natural breathing (quiet tidal breathing) as well as forced breathing (such as during exercise, coughing, or mechanical ventilation) (Deepa et al., 2025). For general insights, the numerical model (Equation 22) can be used to study gas transport within the lung considering physiologically relevant airflow variation during breathing by modeling it as a sinusoidal function i.e., $q(t) = \sin(2\pi t/T_b) = \sin(2\pi\tau)$ following earlier works (Otis et al., 1950; Pradhan and Guha, 2019; Napoli et al., 2022). Salient results are reproduced in (Supplementary Section S3) (Supplementary Figures S2-S5) for pertinent parameters.

The wash-in curve (Supplementary Figure S2) obtained using the numerical model is similar to that reported in previous studies (Wang et al., 2013). It is observed that the wash-in curve reaches a time-periodic state after a few breathing cycles ($\tau \sim 15$) with its frequency corresponding to the breathing cycle, similar to that observed by Chakravarty et al. (2019) in a two-dimensional computational study on alveolar gas transport. The nature of the wash-in curve is observed to change in case the gas source becomes unavailable after a certain time (Supplementary Figure S3). This is relevant when an individual gets exposed to a certain gas source for a finite period of time (τ_{exp}). While the nature of the curve remains similar as long as the exposure takes place, wash-out of the residual gas starts as soon as the exposure stops. The nature of the wash-out curve is again similar to that observed in literature (Paiva and Engel, 1981; Hasler et al., 2019; Darquenne et al., 2022b).

The nature of the wash-in/wash-out curve is also observed to depend on Pe_g, Z as well as St_a. Other parameters remaining constant, an increase in Pe_g results in a larger advective transport (see Figure 3) within the lung leading to a relatively greater $\phi_{g,N}$ at the same time instant and lung generation during inhalation. During exhalation, larger advection leads to faster wash-out and hence, $\phi_{g,N}$ decreases for a larger Pe_g (Supplementary Figures S4a, b). A lower rate of gas exchange (larger Z) within the lung results in a larger $\phi_{g,N}$ at the same time instant and lung generation (Supplementary Figure S4c). Washout from the lung, thus, takes a longer time in case of larger Z. As expected, the time taken for wash-in increases as τ_{exp} becomes larger and the washout starts after the corresponding τ_{exp} ends (Supplementary Figure S4d). However, the qualitative nature of the wash-in and washout curves of $\phi_{g,N}$ remain similar for all τ_{exp}.

The wash-in/wash-out curve is observed to qualitatively change at small St_a. A smaller St_a indicates a much larger breathing time-scale (T_b) with respect to the advective time-scale. The inhaled gas, as such, is able to progress much deeper into the lung during inhalation as St_a is reduced, other parameters remaining same (see Supplementary Figure S5a). Similarly, a smaller St_a allows a longer time for the inhaled gas to get washed out of the lung leading to lower $\phi_{g,N}$ during exhalation such that minimal wash-out occurs after exposure stops (see Supplementary Figure S5b). As St_a increases, wash-out during exposure remains progressively incomplete resulting in some residual $\phi_{g,N}$ within the lung. The residual $\phi_{g,N}$ is again transported along with the airflow after exposure ends. As St_a becomes larger, this transport remains restricted to the upper region of the lung and hence, is washed out relatively fast.

2.3 Particle transport and deposition

Transport of particles within the lung is fundamentally similar to transport of gases in the lung. Here, the term *particle* is used to

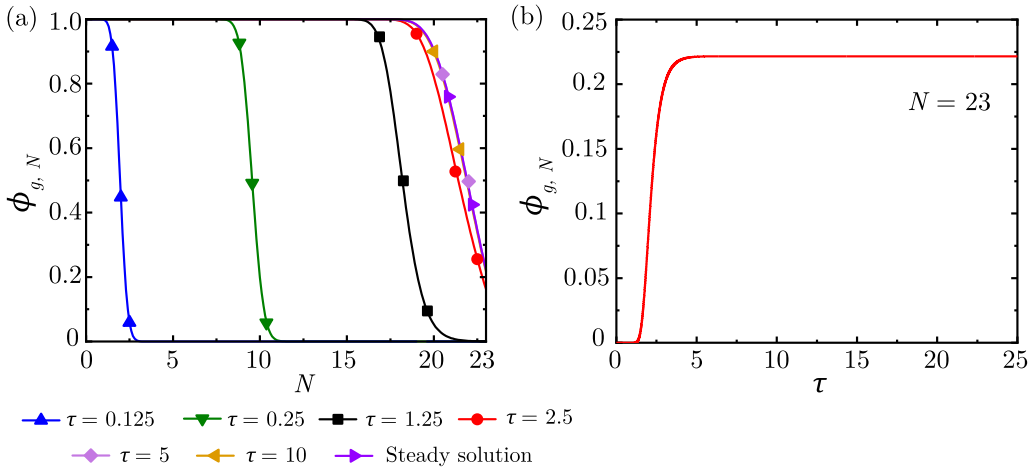

FIGURE 5
(a) $\phi_{g,N}$ within the lung at different time instances **(b)** Temporal change in $\phi_{g,N}$ at $N = 23$. The results are shown for $Pe_{g,pl} = 64500$, $Z = 500$, $St_a = 0.01$, $\alpha = 0.73, \beta = 0.71$. It can be observed that the $\phi_{g,N}$ front advances deeper into the lung as time progresses and reaches a steady-state after approximately $\tau = 5$. The steady-state $\phi_{g,N}$ from the numerical solution matches the $\phi_{g,N}$ obtained from the steady-state theoretical solution.

denote solid particles as well as liquid droplets/aerosols. The one-dimensional transport equation for particles at any location in the idealised lung geometry can be expressed in a similar manner as that for gases (Equation 13) as follows (Chakravarty et al., 2022; Chakravarty et al., 2023; Choi and Kim, 2007; Taulbee and Yu, 1975; Mitsakou et al., 2005; Darquenne and Paiva, 1994) -

$$\frac{\partial\left(Ac_{p,a}\right)}{\partial t}+\frac{\partial\left(Qc_{p,a}\right)}{\partial x}=\frac{\partial}{\partial x}\left(AD_{p,a}\frac{\partial c_{p,a}}{\partial x}\right)-\left(L_d c_{p,a}\right), \tag{25}$$

where, $c_{p,a}$ and $D_{p,a}$ represents the particle concentration (in airways) and particle diffusivity in air, respectively. Q represents the volume flow rate of air in breathing.

A major physiological difference exists between the gas and particle transport mechanisms. While the gas molecules are exchanged between the blood stream and the lung in the alveoli, inhaled particles/droplets are deposited in the airway mucus throughout the lung. Therefore, the gas exchange term in Equation 13 is replaced by a deposition term $(L_d c_{p,a})$ in Equation 25, where L_d is the coefficient of deposition. L_d is calculated taking into account different physical deposition mechanisms viz. diffusional, sedimentation, and impact deposition in the lung airways, as well as diffusional and sedimentation deposition in the alveoli (Chakravarty et al., 2022; Yeh and Schum, 1980; Hofmann, 2011; Devi et al., 2016).

Equation 25 can be expressed in terms of lung generation number (N) assuming a power law variation (see Section 2.2.1) as

$$A_0(2\beta)^N\frac{\partial c_{p,a}}{\partial t}=H\frac{\partial}{\partial N}\left[\left(A_0(2\beta)^N D_{p,a}H\frac{\partial c_{p,a}}{\partial N}\right)-\left(Q_m q(t)\,c_{p,a}\right)\right]-\left(L_d c_{p,a}\right), \tag{26}$$

where, $q(t)$ represents the temporal sinusoidal function accounting for airflow variation during breathing such that $Q = Q_m q(t)$. Equation 26 is reduced to its dimensionless form by multiplying and dividing Equation 26 with $\left(\frac{L_0}{A_0 D_{p,a}}\right)$ and $\left(-\frac{\alpha\ln(\alpha)}{1-\alpha}\right)$, respectively, and using the following scaling parameters (Chakravarty et al., 2022)

$$\tau=\frac{t}{T_b},\phi_{p,a}=\frac{c_{p,a}}{c_{p,a,0}},T_a=\frac{L_0A_0}{|Q_{max}|},St_a=\frac{T_a}{T_b},Pe_{p,a}=\frac{|Q_{max}|L_0}{A_0D_{p,a}},$$
$$D_{p,a}=\frac{k_BTC_S}{3\pi\mu_a d_p}, \tag{27}$$

where, $Pe_{p,a}$ and St_a are the Peclet number for particles (in airways) and Strouhal number for the airways, respectively. $\phi_{p,a}$ and τ denotes the dimensionless particle concentration (in airways) and time, respectively, while the quantities T_a and T_b represents the convective airflow time-scale and breathing time-scale, respectively. The expression of $D_{p,a}$ is based on the Stokes-Einstein relation (Chakravarty et al., 2019), where C_s represents the Cunningham slip correction, T represents the ambient temperature, μ_a denotes air viscosity, and d_p denotes the particle diameter.

The dimensionless equation is expressed as (Chakravarty et al., 2022; Chakravarty et al., 2023)

$$\left(|Pe_{p,a}|St_a(2\alpha\beta)^N\right)\frac{\partial\left(\phi_{p,a}\right)}{\partial\tau}=\frac{\partial F_{p,a}}{\partial N}-\left(L'_d\phi_{p,a}\right), \tag{28}$$

where, L'_d represents the dimensionless form of droplet deposition coefficient (L_d) and $F_{p,a}$ represents the total particle flux in airways. These are expressed as follows -

$$L'_d=L_d\frac{L_0^2}{A_0D_{p,a}}\alpha^N, \tag{29}$$

$$F_{p,a}=\left[\left(\left(\frac{2\beta}{\alpha}\right)^N\left(\frac{1-\alpha}{\alpha(\ln\alpha)}\right)^2\frac{\partial\phi_{p,a}}{\partial N}\right)+\left(|Pe_{p,a}|q(t)\left(\frac{1-\alpha}{\alpha\ln(\alpha)}\right)\phi_{p,a}\right)\right]. \tag{30}$$

Different empirical models available in the literature have been used to estimate L'_d by suitably modifying them to maintain consistency with the present mathematical formulation (see (Chakravarty et al., 2022) for details). The final dimensionless form of these deposition models are expressed as follows (Chakravarty et al., 2022).

Diffusional deposition in the airways:

$$L'_{d,D} = L_{d,D}\frac{L_0^2}{A_0 D_{p,a}}\alpha^N = \left(\frac{L_0}{R_0}\right)^2 (2\alpha)^N (3.66 + 22.305 + 57). \quad (31)$$

Sedimentation deposition in the airways:

$$L'_{d,s} = L_{d,s}\frac{L_0^2}{A_0 D_{p,a}}\alpha^N = \frac{1}{3}\left(\frac{L_0}{R_0}\right)^2 \left(2\alpha\sqrt{\beta}\right)^N S_g \cos(\psi_N), \quad (32)$$

where, S_g is defined as the sedimentation parameter and expressed as

$$S_g = \frac{R_0 \rho_p d_p^3 g}{k_B T}. \quad (33)$$

Impact deposition in the airways:

$$L'_{d,i} = L_{d,i}\frac{L_0^2}{A_0 D_{p,a}}\alpha^N = |Pe_{p,a}|q(t)\ln\left(f_i^N(\theta, St)\right)\frac{(1-\alpha)}{\alpha\ln(\alpha)}. \quad (34)$$

Diffusional deposition in the alveoli:

$$L'_{d,D,alv} = \gamma_N \eta_{D,alv} |Pe_{p,a}| q(t)\left(\frac{1-\alpha}{-\alpha\ln(\alpha)}\right), \quad (35)$$

where, γ_N denotes the fraction of alveolated area in the corresponding generation (Chakravarty et al., 2022) and $\eta_{D,alv}$ denotes the diffusional deposition efficiency in the alveoli. $\eta_{D,alv}$ is expressed as (Devi et al., 2016)

$$\eta_{D,alv} = 1 - \frac{6}{\pi^2}\sum_{k=1}^{\infty}\frac{1}{k^2} exp\left[-\frac{4k^2 t D_p}{d_{eq}^2}\right]. \quad (36)$$

Sedimentation deposition in the alveoli

$$L'_{d,s,alv} = \gamma_N \eta_{s,alv} |Pe_{p,a}| q(t)\left(\frac{1-\alpha}{-\alpha\ln(\alpha)}\right), \quad (37)$$

where, γ_N and $\eta_{s,alv}$ denotes the fraction of alveolated area in the corresponding generation (Chakravarty et al., 2022) and sedimentation deposition efficiency in the alveoli, respectively. $\eta_{s,alv}$ is expressed as (Devi et al., 2016)

$$\eta_{s,alv} = \left[1 + \min\left(\frac{d_s}{d_{eq}}, 1\right)\right]^2 \left[1 - 0.5\min\left(\frac{d_s}{d_{eq}}, 1\right)\right]^2 - 1. \quad (38)$$

The transport equations (Equations 25 and 28, along with Equations 29–38) are formulated based on the assumption that the particle suspension is dilute and that the particles are mono-dispersed, do not undergo coagulation, and are decoupled from airflow in the lung (Kleinstreuer and Zhang, 2010). Based on the inherent physiology, it is also assumed that there is no additional source of particles present within the lung, and the inhaled particles are either deposited in the airway mucus or washed out of the airways. The developed mathematical model has been validated against *in vivo* experimental data of Heyder et al. (1986) for different inhaled, mono-dispersed particle sizes [see Chakravarty et al. (2022) for details]. This justifies the assumptions made in formulating the model.

Figure 6a illustrates the transport of particles within the lung airways in a particular breathing cycle. Once inhaled, the particles are carried along with the airflow inwards into the lung during the inhalation phase of the breathing cycle. The particle concentration ($\phi_{p,a}$) reaches its deepest region in the lung at the end of inhalation. This depends on $Pe_{p,a}$ which is determined by the airflow velocity and particle diffusivity. During the exhalation phase of the breathing cycle, the particles are transported towards the upper regions of the lung and are ultimately washed out of the lung. However, it can be observed from Figure 6a that all inhaled particles may not get washed out in a single breathing cycle leading to some residual $\phi_{p,a}$ within the lung at the end of exhalation. These residual particles are again transported inwards into the lung along with any additional inhaled particles (Chakravarty et al., 2019; Chakravarty et al., 2022).

As discussed, the inhaled particles may also get deposited in the airway mucus while being transported within the lung. As a result of deposition, the net $\phi_{p,a}$ decreases which is apparent from the comparative plot in Figure 6a. The total amount of particle deposited in the airway mucus is shown in Figure 6b for a representative case. It can be observed that the deposition is non-uniform and it increases towards the deep lung (acinar region) reaching a maximum at $N = 22$. This trend of deposition is, however, observed to be dependent on $Pe_{p,a}$, St_a and the exposure duration (Chakravarty et al., 2022). Exposure duration (τ_{exp}) is observed to only quantitatively influence particle deposition (other parameters remaining same) with the total deposition increasing linearly as τ_{exp} becomes longer (see Supplementary Figure S6). However, $Pe_{p,a}$ as well as St_a are observed to qualitatively influence particle deposition as discussed below.

Particles are observed to deposit in the deep lung only when $Pe_{p,a}$ remains in the range of $2.37 \times 10^6 - 3.07 \times 10^{11}$ (see Supplementary Figure S7a). The reason being, at small $Pe_{p,a}$, the advection is not strong enough to carry the particles into the deep lung, whereas at large $Pe_{p,a}$ the particles deposit primarily in the upper airways due to the impaction mechanism (Chakravarty et al., 2022; Hofmann, 2011; Choi and Kim, 2007; Heyder et al., 1986). This range translates to particle diameters of 0.006 μm to 20 μm for normal breathing in a healthy individual (tidal volume of 1000 ml and $T_b = 4$ s). Within this range, deposition in the deep lung increase up to $Pe_{p,a} \sim 10^8$ and then decreases to reach a minimum when $4.29 \times 10^9 < Pe_{p,a} < 1.6 \times 10^{10}$ (particle diameters ~0.4 – 1.2 μm). Beyond this, another increase in deposition in the deep lung take place with a peak at $Pe_{p,a} = 9.03 \times 10^{10}$ (particle diameter of 3 μm) (Chakravarty et al., 2022).

A longer breathing time period (lower St_a) results in *deeper* breaths and lead to greater volume of air (and hence, particles) being inhaled, keeping all other parameters same and vice-versa. This increases the probability of the inhaled particle reaching the deep lung. Consequently, the deposition pattern also shifts towards the deep lung with decrease in St_a (see Supplementary Figure S7c, d). The fraction of particles deposited in the deep lung are, as such, observed to increase as St_a decreases (see Supplementary Figure S7b) (Chakravarty et al., 2022).

The above discussed results are also consistent with the observations of various experimental studies on the effects of inhalation flow rate, particle size and inhalation duration on particle deposition in the lung (Heyder et al., 1986; Kim and Jaques, 2004). Further, the applicability of specific model hypotheses and observations from this study can be experimentally verified in the future (with suitable model augmentations, if required) through focused experiments that have been made possible through experimental advances that can mimic the lung structure and function (Sznitman, 2021; Fishler et al., 2015; Möller et al., 2021; Chen et al., 2025; Kant et al., 2023).

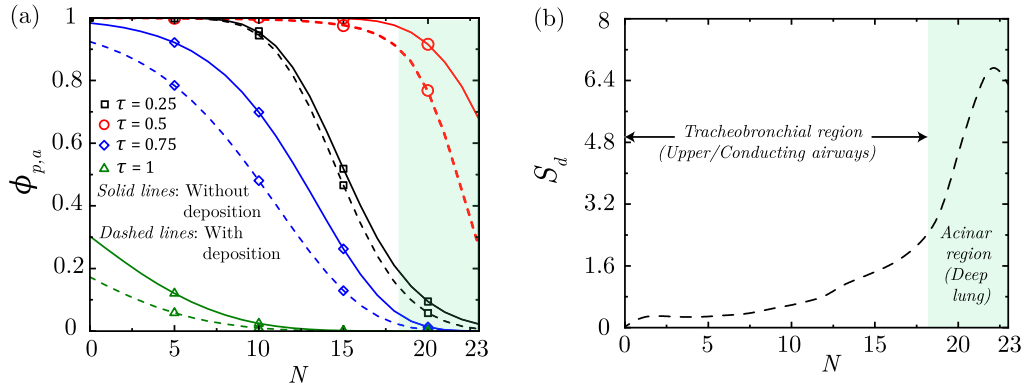

FIGURE 6
(a) Dimensionless particle concentration ($\phi_{p,a}$) within the lung at different instances of a single breathing cycle with and without deposition; the time instances $\tau = 0.25$, $\tau = 0.5$, $\tau = 0.75$ and $\tau = 1$ indicate inhalation peak, inhalation end, exhalation peak and exhalation end, respectively. **(b)** Total droplet deposition ($S_d = \int\int L'_d \phi_{p,a} dV d\tau$) within the lung at the end of exposure as a function of lung generation (N). The results are shown for $Pe_{p,a} = 2.85 \times 10^{10}$, $St_a = 0.0095$ and $\tau_{exp} = 5$. The tracheobronchial region and the acinar (deep lung) regions of the lung are indicated within the plots for better inference.

3 Mucus fluid dynamics

3.1 Mucus clearance

The mass and momentum balance equations of the mucus layer within the lung can be written, based on existing literature (Mauroy et al., 2004; Mauroy et al., 2011; Smith et al., 2008; Karamaoun et al., 2018), as

Mass balance:

$$\frac{\partial A_{m,N}}{\partial t} + \frac{\partial Q_m}{\partial x} = S_{m,N}. \tag{39}$$

Momentum balance:

$$\rho_m \frac{\partial}{\partial t}\left(\frac{Q_m}{A_{m,N}}\right) = -\frac{\partial p_a}{\partial x} + f'_c - f'_{visc}, \tag{40}$$

where f'_c and f'_{visc} are the mucociliary propulsive force and the mucosal viscous resistive force per unit mucosal volume, respectively. The convective mucus transport term is neglected due to low Reynolds number flow in the thin viscous mucus layer. Note that the airway pressure gradient $\frac{\partial p_a}{\partial x}$ is assumed to be imposed in the mucus layer. This is similar to how pressure outside the boundary layer gets imposed within it. $A_{m,N}$ and $S_{m,N}$ are the area of the mucus layer and mass source of the mucus at the N^{th} lung generation. Q_m is the mucus volume flow rate and ρ_m is the density of the mucus. These quantities are defined as

$$A_{m,N} = 2\pi R_N \delta_{m,N} 2^N;\ Q_m = A_{m,N} v_{m,N};\ S_{m,N} = 2\pi R_N G_{m,N} 2^N;$$
$$G_{m,N} = G_{m,0} \psi_g^N,$$

where $\delta_{m,N}$ is the thickness of the mucus layer at the N^{th} lung generation and v_m is the mucus velocity. G_m represents the volumetric mucus source per unit area per unit time. Using these definitions and $H_N = \frac{\partial N}{\partial x}$, the mass balance equation (Equation 39) is re-written in terms of N as

$$\frac{\partial}{\partial t}\left(2\pi R_N \delta_{m,N} 2^N\right) + H_N \frac{\partial}{\partial N}\left(2\pi R_N \delta_{m,N} 2^N v_m\right) = 2\pi R_N G_{m,N} 2^N. \tag{41}$$

Equation 41 can be simplified into

$$\frac{\partial}{\partial t}\left(\delta_{m,N}\right) - \left[\left(\frac{(1-\alpha)}{L_0 \alpha \ln(\alpha) R_N (2\alpha)^N}\right)\frac{\partial}{\partial N}\left(R_N \delta_{m,N} 2^N v_m\right)\right] = G_{m,N}. \tag{42}$$

Similarly, the momentum balance equation (Equation 40) can be converted in terms of lung generation number (N) using the above parameters and the converted equation is expressed as

$$\rho_m \frac{\partial}{\partial t}\left(\frac{Q_m}{A_{m,N}}\right) = \frac{8\pi\mu_a Q_a}{2^N A_0^2 \beta^{2N}} + \frac{k_c \mu_m h_c v_c N_{c0} N'_c}{\delta_{m,N}} - \frac{k_v \mu_m v_m}{\delta_{m,N}^2}, \tag{43}$$

where

$$\frac{\partial p_a}{\partial x} = -\frac{8\pi\mu_a Q_a}{2^N A_0^2 \beta^{2N}},$$
$$f'_c = k_c\left(\mu_m h_c v_c N_{c0} N'_c\right)\left(\frac{1}{\delta_{m,N}}\right),$$
$$f'_{visc} = k_v\left(\frac{\mu_m v_m}{\delta_{m,N}}\right)\left(\frac{1}{\delta_{m,N}}\right).$$

In the expressions above, μ_m is the mucosal viscosity, h_c is the height of each cilia, v_c is the cilia driving velocity scale, N_{c0} is the number of cilia per unit surface area in generation 0, N_c is the number of cilia in generation N, and $N'_c = N_c/N_{c0}$.

In the expression for f'_c, the term in the first parenthesis is the scale of the total mucociliary driving force, the term in the second parenthesis arises due to conversion to force per unit volume, and k_c is the proportionality constant. Similarly, in the expression for f'_{visc}, the term in the first parenthesis is the scale of the viscous shear resistance to mucosal flow, the term in the second parenthesis arises due to conversion to force per unit volume, and k_v is the proportionality constant.

In order to obtain the dimensionless form of Equations 42 and 43, we define the following

$$\tau = \frac{t}{T_b},\ \delta'_{m,N} = \frac{\delta_{m,N}}{\Delta_{m,s}},\ v'_{m,N} = \frac{v_{m,N}}{v_{m,s}}, \tag{44}$$

where T_b is the breathing time scale. $\Delta_{m,s}$ and $v_{m,s}$ are the mucus layer thickness scale and the velocity scale, respectively. These scales

are estimated based on steady-state scalings implied by mass and momentum balance equations. The dominant steady-state scaling is between the last two terms in each of the Equations 42 and 43, which gives

$$\Delta_{m,s} = \sqrt{\frac{k_v G_{m,0} L_0}{k_c h_c v_c N_{c,0}}},\ v_{m,s} = \frac{G_{m,0} L_0}{\Delta_{m,s}}. \tag{45}$$

The dimensionless equations, thus, obtained using the scales defined in Equations 42, 43 can be written as

$$St_m \frac{\partial}{\partial t}\left(\delta'_{m,N}\right) - \left[\frac{(1-\alpha)}{\alpha \ln(\alpha)(2\alpha^2)^N}\frac{\partial}{\partial N}\left(\delta'_{m,N} v'_{m,N}(2\alpha)^N\right)\right] = \psi_g^N, \tag{46}$$

$$Re_m St_m \frac{\partial v'_{m,N}}{\partial t} = P_Q - \left(\frac{N'_c}{\delta'_{m,N}}\right) - \left(\frac{1}{\delta'_{m,N}}\right)\frac{v'_{m,N}}{\delta'_{m,N}}, \tag{47}$$

where $St_m \left(= \frac{T_m}{T_b} = \frac{L_0}{v_{m,s} T_b}\right)$ and $Re_m \left(= \frac{\rho_m G_{m,0} \Delta_{m,s}}{k_v \mu_m}\right)$ are the Strouhal number and Reynolds number for the mucus layer, respectively. The parameter P_Q is defined as $\left(\frac{8\pi\mu_a Q_a \Delta_{m,s}^2}{(2\beta^2)^N A_o^2 k_v \mu_m v_{m,s}}\right)$. Equations 46 and 47 are solved in a coupled manner to obtain the spatio-temporal change in δ'_m and v'_m within the lung. It is initially assumed that δ'_m and v'_m follow a power-law spatial change, similar to the assumptions made for airway length and area (Equation 1), in accordance with the following equations

$$\delta'_{m,N} = \delta'_{m,0}\zeta^N, \tag{48}$$

$$v'_{m,N} = v'_{m,0}\varepsilon^N, \tag{49}$$

where $\delta'_{m,0}$ and $v'_{m,0}$ are the dimensionless mucus thickness and mucus velocity, respectively, at $N = 0$. The magnitudes of ζ and ε in Equations 48, 49 are considered to be 0.9 and 0.87, respectively, based on reported data (Karamaoun et al., 2018). As discussed previously in Section 1 (Equation 2), mucus velocity ($v'_{m,N}$) is assumed to be zero beyond N = 17 due to the absence of appreciable mucociliary transport in the deep lung Mauroy et al. (2011). The spatial change due to the above assumptions is represented in Figure 7a. Note that the mucus velocity has a negative magnitude since mucus flow is in a direction opposite to increasing depth of the lung and becomes zero in the deep lung. N'_c is assumed to vary as ψ_n^N where $\psi_n = \frac{\varepsilon}{\zeta}$. ψ_g is defined as $\frac{\varepsilon\zeta}{\alpha}$.

Solution of the equations indicate that the dimensionless mucus layer thickness (δ'_m) remain almost invariant with time (see Figure 7b). However, the dimensionless mucus velocity (v'_m) undergoes a time-periodic change about a mean value (see Figure 7b), which is in phase with the breathing time-period, after an initial period of transience. Airflow during inhalation resists the mucus transport and hence, mucus velocity reduces during inhalation. The opposite happens during exhalation due to co-current flow of air and mucus. Similar characteristics are observed at all lung generations although the mucus velocity becomes negligible in the deep lung. The transience period is, however, very short and the time-periodic state is reached in a few breathing cycles. Such transience time-period is very small when compared to the time-scale of particle clearance through mucus transport. Hence, it can be safely neglected when modelling particle clearance. This, coupled with the time-periodic nature of mucus velocity, allows us to assume a steady-state magnitude of mucus velocity within the lung when modelling particle clearance (see Section 3.2).

3.2 Clearance of deposited particles

The one-dimensional transport equation for the particles deposited in the lung mucus, by the various deposition mechanisms (see Section 2.3), is formulated considering mucociliary transport and diffusion of the deposited particles in the mucus. It can be expressed in a similar manner to Equation 25 as follows (Chakravarty et al., 2022; Chakravarty et al., 2023)

$$\frac{\partial\left(A_m c_{p,m}\right)}{\partial t} + H\frac{\partial\left(Q_m c_{p,m}\right)}{\partial N} = H\frac{\partial}{\partial N}\left(A_m D_{p,m} H\frac{\partial c_{p,m}}{\partial N}\right) + L_D c_{p,a}\phi_l, \tag{50}$$

where $c_{p,m}$, A_m, Q_m, and $D_{p,m}$ are deposited particle concentration in the mucus, cross-sectional area of the mucus layer at a particular lung generation, volume flow rate of mucociliary transport, and particle diffusivity in the mucus, respectively. It is assumed that the mucus velocity (v_m) and hence, Q_m remains time-invariant (see Section 3.1). ϕ_l is defined as the quantity of particles, which may get deposited, per unit quantity of particles inhaled. The term $L_D c_{p,a}\phi_l$ takes into account the particles introduced into the mucus due to deposition. Equation 50 is converted to a dimensionless form (Equation 52) using scaling defined in Equation 51 below (Chakravarty et al., 2022; Chakravarty et al., 2023)

$$\tau = \frac{t}{T_b},\ \phi_{p,m} = \frac{c_{p,m}}{c_{p,m,0}},\ c_{p,m,0} = \phi_l c_{p,a,0}\frac{A_0}{A_{m,0}},\ T_m = \frac{L_0}{|v_{m,0}|},$$
$$St_m = \frac{T_m}{T_b},\ Pe_{p,m} = \frac{|v_{m,0}|L_0}{D_{p,m}},\ D_p = \frac{k_B T}{3\pi\mu_m d_p}. \tag{51}$$

$$|Pe_{p,m}|\left(2\alpha\zeta\sqrt{\beta}\right)^N St_m\frac{\partial\phi_{p,m}}{\partial\tau} = \frac{\partial F_{p,m}}{\partial N} + \left(L'_D\frac{D_{p,a}}{D_{p,m}}\phi_{p,a}\right), \tag{52}$$

where $\phi_{p,m}$, $Pe_{p,m}$, and St_m are the dimensionless particle concentration in the mucus, particle Peclet number, and mucus layer Strouhal number, respectively. Also note that $Pe_{p,m}$ refers to the particle Peclet number at $N = 0$ only. T_m denotes the time-scale for mucociliary transport. $D_{p,m}$ is estimated using the Stokes-Einstein relation, where μ_m and d_p are the viscosity of the mucus and the particle diameter, respectively. The last term on the right hand side of Equation 52 is the dimensionless particle source due to deposition. The flux term in Equation 52 is represented as

$$F_{p,m} = \left[\left(\left(\frac{2\zeta\sqrt{\beta}}{\alpha}\right)^N\left(\frac{1-\alpha}{\alpha\ln(\alpha)}\right)^2\frac{\partial\phi_{p,m}}{\partial N}\right) - \left(|Pe_{p,m}|\left(2\varepsilon\zeta\sqrt{\beta}\right)^N\phi_{p,m}\right)\right]. \tag{53}$$

The particles that are inhaled into the lung are deposited in the respiratory mucus during breathing by various mechanisms (see Section 2.3) (Pedley, 1977; Guha, 2008; Kleinstreuer and Zhang, 2010). The deposited particles diffuse in the mucus layer and are also simultaneously transported upstream via mucociliary advection (Cu and Saltzman, 2009). However, mucociliary advection is appreciable only in the conducting airways of the lung ($N < 18$) and is negligible in the deep lung ($N \geq 18$) (Karamaoun et al., 2018). Results obtained by solving Equations 50, 52, along with Equation 53, show that the

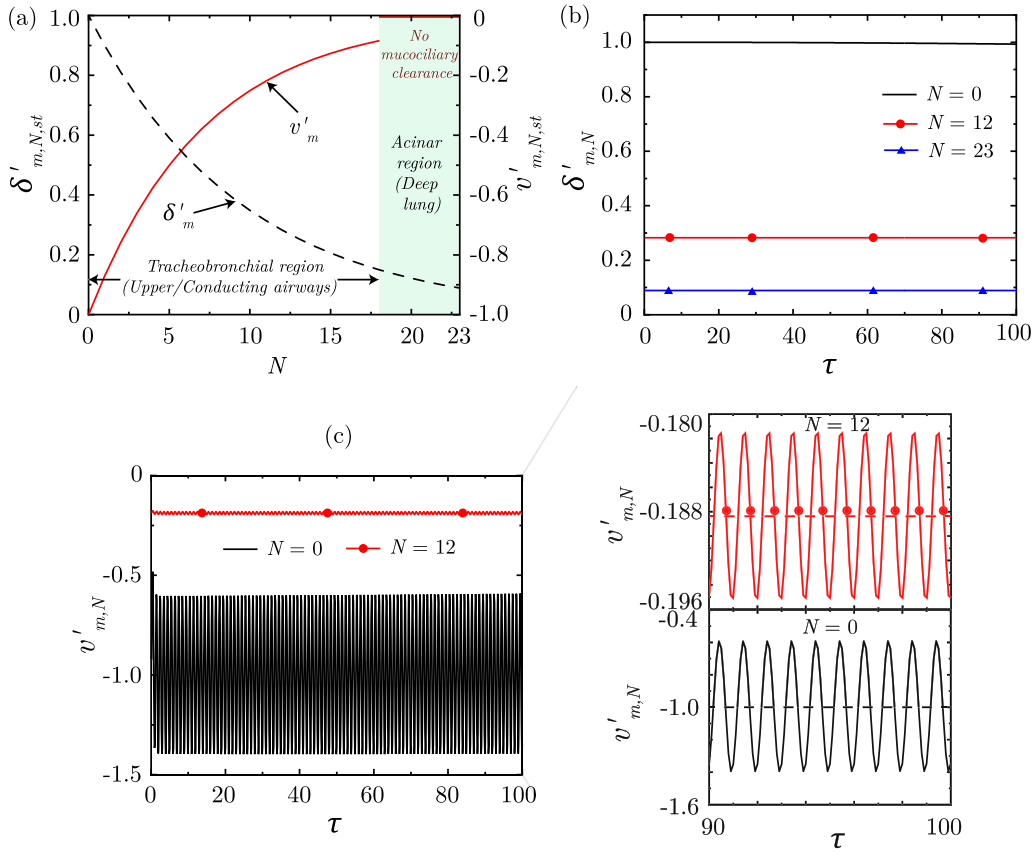

FIGURE 7
(a) Variation of dimensionless, steady-state magnitudes of mucus layer thickness ($\delta'_{m,N,st}$) and mucus velocity ($v'_{m,N,st}$) along the lung generations (N). The thickness and velocity are scaled following Equation 44. For reference, the mucus layer thickness remains in the range of 10 – 30 μm in the trachea, while it becomes 2 – 5 μm in the distal generations (Karamaoun et al., 2018), consistent with the model predictions. Temporal change in **(b)** $\delta'_{m,N}$ and **(c)** $v'_{m,N}$ at three different lung generations ($N = 0,12,23$). The results are shown considering $Re_m = 0.001, St_m = 359.7122, \alpha = 0.73, \beta = 0.71, P_Q = sin(\omega\tau)/(2\beta^2)^N$.

particle concentration in the mucus ($\phi_{p,m}$), at the end of the exposure duration ($\tau = 5$), qualitatively follows particle deposition S_d (see Supplementary Figures S8a, b).

Particles deposited in the conducting airways are transported upstream towards the mouth ($N = 0$) due to mucociliary advection. This results in higher $\phi_{p,m}$ in the upper airways (lower N), as time progresses, primarily due to smaller mucus volume in the upper airways. Eventually, the particles are washed out of the respiratory tract (see Supplementary Figure S8a) along with the mucus. The temporal change in $\phi_{p,m}$ at the mouth (inset Supplementary Figure S8a) also corroborates this conclusion. In contrast, the particles deposited in the deeper generations ($N \geq 18$) is not subjected to mucociliary transport. Therefore, $\phi_{p,m}$ in the deep lung undergoes a gradual change due to weak diffusive transport (see inset Supplementary Figure S8a). As such, particles deposited in the deep lung can persist for a much longer time as compared to those deposited in the upper airways (Chakravarty et al., 2022; Chakravarty et al., 2023). Hence, particles deposited in the distal lung persist for a long time and the resulting health complications are very difficult to manage. This, however, becomes beneficial in case of therapeutic drugs.

4 Pathogen infection dynamics

Pathogens are introduced into the LRT through the carrier particles (or droplets) which are transported in the respiratory tract along with airflow. The carrier particles (or droplets) may be inhaled or formed *in-vivo* through aerosolization of respiratory mucosa (Chakravarty et al., 2023; Darquenne et al., 2022a). The carrier particles (or droplets) deposit in the mucosa of the LRT (see Section 2.3), thereby, seeding an infection. The deposited particles (or droplets) are also simultaneously cleared through advective-diffusive transport (see Section 3.2). The infection - once seeded - may grow, spread and decay depending on various pathogen-specific parameters and the host's immune responses. Modeling the dynamics of a pathogen infection within the respiratory tract, thus, requires simultaneous consideration of all the above mechanisms.

4.1 Pathogen transport in mucus

The one-dimensional pathogen transport equation within respiratory mucosa, thus formulated, is represented in its dimensionless form as (Chakravarty et al., 2023)

$$Pe_{pt,m}\left(2\alpha\zeta\sqrt{\beta}\right)^{N} St_m \frac{\partial \phi_{pt,m}}{\partial \tau} = \frac{\partial}{\partial N}\left[\left(\left(\frac{2\zeta\sqrt{\beta}}{\alpha}\right)^{N}\left(\frac{1-\alpha}{\alpha\ln(\alpha)}\right)^{2}\frac{\partial \phi_{pt,m}}{\partial N}\right) - \left(Pe_{pt,m}\left(2\varepsilon\zeta\sqrt{\beta}\right)^{N}\phi_{pt,m}\right)\right] + \left(L_D'\frac{D_{p,a}}{D_{pt,m}}\phi_{p,a}\right) + \left(2\alpha\zeta\sqrt{\beta}\right)^{N}\left(p_0 I - c_l\phi_{pt,m}\right), \tag{54}$$

where $\phi_{pt,m}$, $Pe_{pt,m}$ and St_m are the dimensionless pathogen concentration in mucus, pathogen Peclet number and mucus Strouhal number, respectively. Equation 54 is similar to Equation 52 except the last term on the right hand side of Equation 54 which accounts for the pathogen-specific infection kinetics using a modified target-cell limited model (Chakravarty et al., 2023) that is developed based on applicability of this approach in predicting previous experimental data (Quirouette et al., 2020; Baccam et al., 2006; Néant et al., 2021).

The modified target-cell limited model (Equations 55–57) assumes that the target cells are infected depending on the pathogen-specific infection rate and the local pathogen concentration (see Equation 55). The infected target cells remain in an eclipse phase for a certain duration before becoming infectious (Equation 56) after which they produce new pathogens for a certain time-span before undergoing apoptosis (Equation 57). The corresponding equations are expressed as follows:

$$\frac{\partial T}{\partial \tau} = -I_r T\phi_{pt,m}, \tag{55}$$

$$\frac{\partial E}{\partial \tau} = \left(I_r T\phi_{pt,m}\right) - \left(\frac{1}{\tau_E}E\right), \tag{56}$$

$$\frac{\partial I}{\partial \tau} = \left(\frac{1}{\tau_E}E\right) - \left(\frac{1}{\tau_I}I\right). \tag{57}$$

T, E and I in the above equations represent the fraction of uninfected target cells, infected cells in the eclipse phase and infectious cells, respectively. I_r denotes the dimensionless infection rate. τ_E and τ_I are the dimensionless time-periods of the eclipse phase and infectious phase, respectively. p_0 and c_l in Equation 54 denote the dimensionless pathogen production rate of new pathogens from the infectious cells and the dimensionless clearance rate of pathogens due to various non-specific clearance mechanisms, respectively (Quirouette et al., 2020; Baccam et al., 2006). The relevant parameters are defined as (Chakravarty et al., 2023)

$$p_0 = \frac{L_0^2}{D_{pt,m}}\frac{p}{c_{pt,m,0}},\ c_l = \frac{L_0^2}{D_{pt,m}}c,\ I_r = \beta c_{pt,m,0}T_b,\ \tau_E = \frac{T_E}{T_b},\ \tau_I = \frac{T_I}{T_b}, \tag{58}$$

where $c_{pt,m}$ is the dimensional pathogen concentration and $c_{pt,m,0}$ is the initial $c_{pt,m}$ at $N = 0$. p, c_l and β are the dimensional rate of pathogen replication, pathogen clearance and infection, respectively. T_E and T_I are the time-scales for the eclipse phase and the infectious phase, respectively.

4.2 Immune response to an infection

A simplified immune response model (Chakravarty et al., 2023), coupled with the infection kinetics model, is utilised to understand the impact of human body's immune response to pathogen infections in the respiratory tract. The model has been formulated based on available experimentally-validated mathematical frameworks (Dobrovolny et al., 2013; Cao et al., 2015; Quirouette et al., 2020) and considers the effects of interferons, antibodies as well as cytotoxic T-lymphocytes. The specific mathematical models for the individual immune responses are discussed in the following sections.

4.2.1 Interferon response

Interferons are assumed to affect infection progression by attenuating replication of the pathogens. The pathogen replication rate (p_0') is, thus, reduced in presence of interferons and is determined as

$$p_0' = \left(1 - \frac{F}{F+f}\right)p_0, \tag{59}$$

where p_0 is the pathogen replication rate in absence of interferons (see Equation 54) and f is the interferon fraction required to halve the replication rate. F is the interferon fraction present in the body (relative to the maximum amount interferons that may be present) and it is assumed to vary with time as

$$F = \frac{2}{e^{-\lambda_{g,i}\left(\tau-\tau_{p,i}\right)} + e^{\lambda_{d,i}\left(\tau-\tau_{p,i}\right)}}, \tag{60}$$

where $\lambda_{g,i}$ and $\lambda_{d,i}$ are the dimensionless rates of interferon growth and decay, respectively. $\tau_{p,i}$ is the dimensionless time at which interferon fraction reaches its maxima.

4.2.2 Antibody response

Antibodies act by neutralising the pathogens present in the body. The pathogen clearance rate (c_l in Equation 54) is, thus, enhanced due to antibodies and is determined as

$$c_l' = c_l + k_A' Ab, \tag{61}$$

where c_l' is the enhanced clearance rate due to antibodies and k_A' is the dimensionless binding affinity of antibodies to the pathogens. Ab is the antibody fraction present in the body and it varies with time as

$$Ab = \frac{1}{1 + \left(\frac{1}{Ab_0} - 1\right)e^{-\lambda_{g,a}\tau}}, \tag{62}$$

where $\lambda_{g,a}$ is the dimensionless antibody growth rate and Ab_0 is the initial antibody fraction present in the body.

4.2.3 T–lymphocyte response

The cytotoxic T–lymphocytes act by directly attacking the infected cells. Equations 56, 57 are, thus, modified when T–lymphocytes are present as

$$\frac{\partial E}{\partial \tau} = \left(I_r T\phi_{pt,m}\right) - \left(\frac{1}{\tau_E}E\right) - \left(k_c' T_l\right)E, \tag{63}$$

$$\frac{\partial I}{\partial \tau} = \left(\frac{1}{\tau_E}E\right) - \left(\frac{1}{\tau_I}I\right) - \left(k_c' T_l\right)I, \tag{64}$$

where k_C' represents the dimensionless rate of infected cells neutralisation by the T–lymphocytes. T_l is the fractional amount of T–lymphocytes present at any time and is determined as

$$T_l = \frac{2}{e^{-\lambda_{g,t}\left(\tau-\tau_{p,t}\right)} + e^{\lambda_{d,t}\left(\tau-\tau_{p,t}\right)}}, \tag{65}$$

where $\lambda_{g,t}$ and $\lambda_{d,t}$ are the dimensionless rates of T–lymphocyte growth and decay, respectively. $\tau_{p,t}$ is the dimensionless time at

which amount of T–lymphocytes present in the body reaches its maxima.

4.3 Infection progression

The pathogen transport model (Sections 4.1, 4.2) coupled with the particle transport and deposition model (Section 2.3) have been utilised to study the dynamics and progression of a SARS-CoV-2 infection in a human LRT (Chakravarty et al., 2023). The predictions of this model has been observed to appreciably predict viral load dynamics available from patient data (Néant et al., 2021; Wang et al., 2020), highlighting the potential future clinical utility of this mathematical model. It is assumed during this analysis that pathogen-loaded droplets are present in the naso-pharyngeal region of the respiratory tract. These droplets may be a combination of droplets inhaled from the environment (which have not deposited in the upper respiratory tract) and those formed due to aerosolization of nasopharyngeal mucosa, and are inhaled into the trachea during breathing. No other source of droplets are considered.

It is observed from the analysis that pathogen (SARS-CoV-2) concentration in mucus ($\phi_{pt,m}$), at the end of the inhalation, is qualitatively similar to droplet deposition characteristics. This is due to a significantly shorter time-scale of droplet deposition, as compared to pathogen infection and clearance from the LRT (Chakravarty et al., 2023). As droplet inhalation stops, mucociliary clearance transports the pathogens deposited in the upper airways of the LRT ($N < 18$) upstream towards the trachea ($N = 0$). This can be inferred from the spatial change in ($\phi_{pt,m}$) with time (see Supplementary Figure S9a). This mechanism washes out the pathogens from the upper airways as long as washout dominates over pathogen replication. Once pathogen replication starts to dominate, $\phi_{pt,m}$ is observed to again increase with time indicating infection growth within the LRT (Supplementary Figures S9a, b).

In contrast to pathogens deposited in airways, pathogens deposited in the deep lung ($N \geq 18$) are transported only through diffusion since mucociliary clearance is negligible in the deep lung. The dynamics of $\phi_{pt,m}$ in the deep lung is, thus, governed by the weaker diffusive transport (compared to mucociliary clearance) and pathogen kinetics only. As a result, deep lung deposition of pathogens leads to longer persistence times. This increases the probability of an infection becoming severe causing serious diseases (pneumonia, acute respiratory distress syndrome etc.). In addition, the thin surfactant layer lining the deep lung increases the possibility of the pathogens entering the blood stream.

The LRT infection is observed to grow as long as pathogen replication dominates over pathogen clearance. Once clearance becomes stronger, infection starts to recede ($\phi_{pt,m}$ decreases) with time (see Supplementary Figure S9b). This results in a peak infectious state beyond which infection starts to resolve. The peak infectious state and the infection resolution time is observed to be dependent on several fluid dynamics, physiological as well as infection parameters (see Chakravarty et al. (2023) for details). The analysis reveals that the major impact is due to immune responses, paticularly antibodies (Supplementary Figure S10a) and cytotoxic T-lymphocytes (Supplementary Figure S10b), which reinforces the critical role played by vaccination in preventing infection severity.

5 Discussion

5.1 Utility and limitations of 1D models

High resolution computational simulations of the complete respiratory tract becomes difficult due to the geometrical complexity of the respiratory tract (Karamaoun et al., 2018; Ghorui et al., 2024). Analyses have shown that the transport phenomena within the respiratory tract has a time-periodic nature which enables 1D approximations with reasonable accuracy (Chakravarty et al., 2019). Simplified 1D computational models would be reasonable when the focus is to capture the key trends of droplet/particle/pathogen transport and deposition for the complete respiratory tract. While such simplified models cannot account for the effects of heterogeneity in the lung, it is a tractable approach and can help understand some of the key trends dependent on the entire respiratory tract (see Sections 2 and 3). Investigation of pulmonary drug delivery using a simplified 1D model (see Sections 2.3 and 3.2) has provided information regarding spatio-temporal drug deposition characteristics throughout the respiratory tract and also suggested ways of enhancing drug delivery efficacy (Chakravarty et al., 2022). The pathogen infection model (see Section 4.1) has been utilised to study the spatio-temporal evolution of SARS-CoV-2 infection in a human respiratory tract and provided useful information on the role played by various physiological and fluid dynamic parameters on infection characteristics (Chakravarty et al., 2023). Similar investigations can be carried out considering other viral infections as well.

It is worthwhile to note that the 1D single trumpet model does not fully resolve complicated flow patterns in the URT or the effect of heterogeneity in the lungs. This limits the use of 1D models in studying the effects of anatomical variability of the lung - multi-path models (Kundu and Panchagnula, 2023; 2025) and high-fidelity 3D simulations (Bartol et al., 2024) prove to be more well-suited in this regard. One workaround is through appropriate consideration of variation in the geometric parameters of reduced-order 1D models. Devi et al. (2016) used this approach in a 1D trumpet model to identify the particle sizes which showed the least inter-subject variability in deposition. In a recent study, Mate-Kole et al. (2024) employed machine learning techniques to enhance uncertainty quantification and sensitivity analysis in the ICRP model for inhaled radionuclides. A second approach could be through modelling of a network of dichotomously branched heterogeneous lung by approximating each branch as a 1D tube with similar governing equations as the trumpet model. This is reported before (Hasler et al., 2019; Kundu and Panchagnula, 2023) and also summarized in Section 5.3.3, below.

5.2 Dimensionless numbers determining lung function

Dimensionless numbers give an understanding of the dominant physics in the governing equations and therefore, the lung function. This is evident from the equations and results summarized in this article in the previous sections. Table 2 summarizes the dimensionless numbers that govern the various lung functions - airflow, gas exchange, particle deposition and clearance, and

infection dynamics - and their typical physiological magnitudes. The magnitude of infection dynamics parameters listed are relevant for a typical SARS-CoV-2 infection (Chakravarty et al., 2022) and are subject to variations while modeling other respiratory infections. These dimensionless numbers listed in Table 2 could form the basis of constructing a *virtual disease landscape* discussed in Section 6 below.

5.3 Optimal branching of the lung

One of the questions of interest is whether the lung morphology has developed to be optimal for certain function(s). And if so how would deviations from standard morphology potentially lead to pathologies? The primary function of the lung is gas exchange. Thus, its morphology might be optimal for air flow and/or gas exchange. The former has been reported in literature (see Section 5.3.1 below) and some insights on the latter are also discussed below (see Section 5.3.2). Asymmetry of the branching structure of the lung may also affect optimality (see Section 5.3.3).

While particle deposition and clearance in the lung has been extensively studied, more research is needed to determine whether the lung morphology is optimal to minimize particle deposition from inhaled air and to maximize particle removal via mucus clearance - necessary actions from the perspective of disease prevention. We note that particle deposition is different from gas exchange, although the governing equations are similar (see Sections 2.3 and 1). This is because, particles are not absorbed easily into the bloodstream like, say, oxygen because they are much bigger in size. Instead, particles deposit in the mucosal layer and mucus clearance transports the particles out of the lung.

5.3.1 Optimization based on air flow

There are at least two ways to investigate whether the lung morphology is optimal to minimize resistance to air flow. The first approach involves an analysis where the total length and volume of different dichotomous trees being compared are held fixed. Then α and β (see Equation 1) can be optimized such that the total flow resistance is minimized. It is to be noted that the physiological values of α and β are close to the optimal values Mauroy et al. (2004); Weibel and Gomez (1962).

A second alternate approach is to fix the dimensions of the zeroth generation (trachea) and then keep adding dichotomous generations. Clearly, the length and volume will keep increasing as one considers scenarios with increasing number of generations. Hence, to compare across these scenarios with different number of generations, one can do a comparison of a dimensionless resistance normalized by the resistance of straight tube of the same length and volume as a particular tree network being analyzed. This is similar to the concept of drag coefficient for flow over objects. To that end, consider a straight tube of the same length x and the same total volume as a trumpet model with N generations. Assuming parabolic flow in this equivalent straight tube, its flow resistance R_s is given by Equation 66 as

$$R_s = R_0\left(\frac{1-\alpha^{N+1}}{1-\alpha}\right)^3\left(\frac{1-2\alpha\beta}{1-(2\alpha\beta)^{N+1}}\right)^2. \tag{66}$$

The dimensionless ratio, R^+, of R_s to the resistance of a trumpet model with N generations (R_{tN}) is given by

$$R^+ = \frac{R_s}{R_{tN}} = R_0\left(\frac{1-\alpha^{N+1}}{1-\alpha}\right)^3\left(\frac{1-2\alpha\beta}{1-(2\alpha\beta)^{N+1}}\right)^2\left(\frac{1-\left(\frac{\alpha}{2\beta^2}\right)}{1-\left(\frac{\alpha}{2\beta^2}\right)^{N+1}}\right). \tag{67}$$

Maximizing R^+ (i.e., minimizing the relative value of R_{tN}) leads to the optimal values of α and β. It follows from Equation 67 that the optimal value of $\alpha = 0.78$ for $N = 23$ and $\beta = \alpha^2$ (Kou et al., 2014), which is close to the physiological value.

5.3.2 Optimization based on gas exchange

Optimization of lung structure for gas exchange is another consideration (Sapoval et al., 2002). Similar to the second approach for flow resistance-based optimization, one can optimize the resistance to the impalement of gas into the deep lung. To that end, consider the total resistance R_{ct} to the flux of concentration. We define R_{ct} as the concentration difference per unit concentration flux. We compare the trumpet configuration concentration resistance R_{ct} to the concentration resistance R_{cs} in a straight tube of the same length and volume. Following theoretical solutions as presented earlier, we get

$$R_c^+ = \frac{R_{cs}}{R_{ct}} = \left(\frac{1-\alpha^{N+1}}{1-\alpha}\right)^3\left(\frac{1-2\alpha^3}{1-(2\alpha^3)^{N+1}}\right)^3(2\alpha^3)^N\left(\frac{1-\exp\left(-Pe_{st}\right)}{1-\exp\left(Pe_{g,pl}\left(\delta^N-1\right)\right)}\right), \tag{68}$$

where $\beta = \alpha^2$ has been used and R_c^+ is the ratio of concentration resistances discussed above. Pe_{st} is the Peclet number of the straight channel of same length, volume, and pressure difference as the trumpet channel. The concentration at $N = 23$ is taken to be zero for all practical purposes and the inlet concentration is a specified constant value. Equation 68 shows that R_c^+ is maximized for $\alpha > 2/3$, once again in the physiologically relevant range.

5.3.3 Asymmetry and optimality

Although the aforementioned optimality results assumed symmetric branching, those results may be regarded to be relevant in the "average" sense. An important feature of airway branching structure is also its asymmetry. While a majority of human airway models have assumed a simplified morphology of the lung by considering symmetric bifurcations (Weibel et al., 1963), careful analysis of morphometric measurements have shown that the bifurcations are in fact asymmetrical in nature (Raabe, 1976). Surprisingly, there lies a consistency in the degree of asymmetry across all generations, although it varies from species to species (Majumdar et al., 2005). Studies on investigating the optimal degree of asymmetry have led to interesting results (Miguel, 2016; 2022; Florens et al., 2011; Mauroy et al., 2004; Kundu and Panchagnula, 2023). Mauroy et al. (2004) have shown that a mechanically optimal lung is vulnerable to broncho-constriction. Florens et al. (2011) showed how oxygenation times start decreasing sharply as the degree of asymmetry is increased beyond a critical point.

Through deterministic asymmetric multi-path models of the bronchial trees, Kundu and Panchagnula (2023) studied the optimality of the lung as a multi-functional organ. Their findings suggest that the number of terminal bronchioles, which is correlated to the gas exchange surface area, is maximized

10.3389/fphys.2025.1635983

TABLE 2 Non-dimensional numbers and their physiological magnitudes encountered during airflow, gas exchange, particle deposition and clearance, and infections in the respiratory tract. These numbers are defined in the respective sections of this article.* The magnitudes corresponding to infection dynamics are relevant for a typical SARS-CoV-2 infection.

Phenomena	Dimensionless parameter	Definition	Physiological magnitude
Airflow	Re	Reynolds number (Section 2.1)	$\sim 10^3 - 6 \times 10^{-3}$
	Wo	Womersley number (Section 2.1)	~6 – 0.1
	α	Length-change factor (Equation 1)	0.73
	β	Area-change factor (Equation 1)	0.71
	r	Branching asymmetry parameter (Section 5.3.3)	0 – 0.5
Gasexchange	Pe_g	Gas-phase Péclet number (Equation 21)	~1000 – 65000
	St_a	Strouhal number (air) (Equation 21)	~0.001 – 0.1
	Z	Gas exchange parameter (Equation 17)	~500 – 2500
			$Z_{cr} = 2295.827$
	τ_{exp}	Dimensionless exposure time (Section 2.2.2)	5
Particle deposition and clearance	$Pe_{p,a}$	Particle Péclet number (air) (Equation 27)	$\sim 10^7 - 10^{12}$
	$Pe_{p,m}$	Particle Péclet number (mucus) (Equation 51)	$\sim 10^7 - 10^8$
	St_a	Strouhal number (air) (Equation 27)	~0.001 – 0.1
	St_m	Strouhal number (mucus) (Equation 51)	~100 – 1500
	τ_{exp}	Dimensionless exposure time (Section 2.3)	5
	ζ	Mucus layer thickness change factor (Equation 2)	0.9
	ϵ	Mucus layer velocity change factor (Equation 2)	0.87
*Infection dynamics**	p_0	Pathogen production rate (Equation 58)	$3.8 \times 10^{16} - 5.62 \times 10^{17}$
	c_l	Clearance rate (Equation 58)	$0 - 3.79 \times 10^8$
	f	Half-replication rate interferon fraction (Equation 59)	0.2 – 1
	$\tau_{p,i}$	Interferon fraction peak time (Equation 60)	$2.16 \times 10^4 - 19.44 \times 10^4$
	$\lambda_{g,i}$	Interferon growth rate (Equation 60)	9.26×10^{-5}
	$\lambda_{d,i}$	Interferon decay rate (Equation 60)	4.63×10^{-5}
	k'_A	Antibody-pathogen binding affinity (Equation 61)	$0 - 9.1 \times 10^8$
	Ab_0	Initial antibody concentration (Equation 62)	0.001 – 0.005
	$\lambda_{g,a}$	Antibody growth rate (Equation 62)	3.472×10^{-5}
	k'_C	T-lymphocyte cell neutralisation rate (Equations 63, 64)	$0 - 10^{-3}$
	$\tau_{p,t}$	T-lymphocyte peak time (Equation 65)	$8.64 \times 10^4 - 34.56 \times 10^4$
	$\lambda_{g,t}$	T-lymphocyte growth rate (Equation 65)	9.26×10^{-5}
	$\lambda_{d,t}$	T-lymphocyte decay rate (Equation 65)	4.63×10^{-6}

at symmetry (branching asymmetry parameter $(r) = 0.5$; see Supplementary Figure S11a). The volume occupied by the conducting airways is minimized at symmetry, suggesting the most compact design ($r = 0.5$; see Supplementary Figure S11b). The viscous resistance to air-flow, which should be as low as possible in an optimal lung, is also minimized for a symmetrically branched bronchial tree (see Supplementary Figure S11c). Breathing, the primary function of the lung, is thus optimized for a symmetrically branched bronchial tree based on these three parameters. Therefore, perfectly symmetric bifurcations appear to be the best design for the airways.

However, airway structure in the respiratory system is inherently asymmetric. This is necessitated due to the role played by airway asymmetry in particle filtration - the secondary function of the lung. As aerosol-laden air is inhaled, the particles get deposited in the airways through three main physical mechanisms - diffusion, impaction and sedimentation (Chakravarty et al., 2023; Chakravarty et al., 2022; Kundu and Panchagnula, 2023). Kundu and Panchagnula (2023) have shown that for a finitely asymmetric bronchial tree, the particles get maximally deposited in the non-terminal branches of the lung, thereby protecting the deep lung from getting exposed to foreign particles (see Supplementary Figure S11d). The degree of asymmetry which theoretically maximizes this particle filtration efficiency is very close to that measured in human lung (Majumdar et al., 2005).

Thus, although symmetric branchings are the most optimal for maximizing gas exchange surface area, volume occupied and fluid dynamic resistance, asymmetry can maximize particle filtration by enhancing tracheo-bronchial deposition. This shift from mechanical optimality can enhance the protective mechanism of the airways.

5.4 Transition between convection and diffusion dominant regions

The concentration profiles during inhalation (e.g., Supplementary Figure S1) show that in the upper generations of the lung the gas transport (e.g., of oxygen) is convection dominated. The concentration profile appears almost constant; this is called the "conductive" region of the lung. In the deeper generations, the concentration profile is diffusion dominated. It is characterised by lower concentrations with very small gradients. The concentration profile shows a distinct transition between these two regions. The location of this transition can be theoretically estimated in the limiting case of steady state profile as discussed below.

It follows from Equation 15 that

$$\left(Q - D_g \frac{\partial A_x}{\partial x}\right) \frac{\partial c_{g,x}}{\partial x} - A_x D_g \frac{\partial^2 c_{g,x}}{\partial x^2} = 0. \tag{69}$$

The last term is the diffusion-like term with an effective diffusion coefficient $A_x D_g$ that depends not only on gas diffusion D_g but also on the cross-sectional area A_x of the lung. Thus, increasing area of the lung enhances the effective diffusive transport in deep lung.

The first two terms in Equation 69 are convection-like terms. Of these, the term involving Q is the familiar flow-based convective transport term. The second term involving $\frac{\partial A_x}{\partial x}$ is present only because A_x is not constant in the lung. This term behaves like a pseudo-convective term with an effect that is equivalent to a flow from deeper generations to the mouth (note: $\frac{\partial A_x}{\partial x} > 0$), i.e., like a reverse flow during inhalation. This has an effect of making the concentration profile look like a convection-dominated flow (near constant concentration profile) but in the reverse direction even in the so-called diffusion-dominated region (see Supplementary Figure S1). Thus, it should be expected that the convection-like term based on Q would dominate the upper generations of the lung ("conductive region"), while the convection-like term based on A_x would dominate the deeper generations of the lung ("diffusive region"). The transition location is influenced by a competition between these two mechanisms, as shown below.

For the profile in the transition region, there will be an inflection point (see Figure 8). Consequently, at the inflection point in the plot of $c_{g,x}$ vs. x, we have $\frac{\partial^2 c_{g,x}}{\partial x^2} = 0$ without $\frac{\partial c_{g,x}}{\partial x}$ becoming zero. This is possible when (Paiva et al., 1976)

$$Q = D_g \frac{\partial A_x}{\partial x} = D_g \frac{\partial N}{\partial x} \frac{\partial A_N}{\partial N}. \tag{70}$$

Substituting relevant expression in Equation 70 and solving for the generation number N_I at the inflection point for a given constant flow rate Q, we get

$$N_I = \frac{\ln\left[-\frac{1}{Pe_g}\left(\frac{1-\alpha}{\alpha}\right)\frac{\ln(2\beta)}{\ln\alpha}\right]}{\ln\left(\frac{\alpha}{2\beta}\right)}. \tag{71}$$

Figure 8 shows the change in location of the transition zone (in terms of N_I) for a range of Pe_g as obtained using Equation 71. It can be observed that the transition zone progressively moves inwards into the lung with increase in convection (larger Pe_g). This can be corroborated with the gas concentration profiles shown in Figure 3. Furthermore, the breadth of the transition region can also be estimated. We note that around the inflection point the convection and diffusion terms must be of the same order

$$Q c_{g,x} \sim A_x D_g \frac{\partial c_{g,x}}{\partial x}. \tag{72}$$

Inserting scales in Equation 72, we get that the width δ_I of the transition region around the inflection point should be such that

$$Pe_I = \frac{Q\delta_I}{A_I D} \sim \mathcal{O}(1). \tag{73}$$

Equation 73 gives an estimate for δ_I.

5.5 Nitrogen washout

Single or multiple-breadth washout (SBW or MBW) of nitrogen (N_2) is one of the tests used to quantify the degree of heterogeneity in the ventilation of the lung. Since N_2 is present in the air, there is an equilibrium concentration in the deep lung during regular breathing. During the test, the subject breathes pure oxygen (O_2) so that N_2 starts getting washed out of the lung. During each exhalation, the concentration of N_2 vs. time has a profile similar to that in Figure 9. The concentration of N_2 coming out is low at the beginning of exhalation since that is the gas (mostly O_2) from the upper generations of the lung. The N_2 concentration goes up when N_2 from deep lung starts exiting. The slope of this final phase of the graph is not zero (Krogh and Lindhard, 1917; Crawford et al., 1985; Paiva, 1989; Engel and Paiva, 1981). This is the slope of the "alveolar plateau." It has been found that this slope is indicative

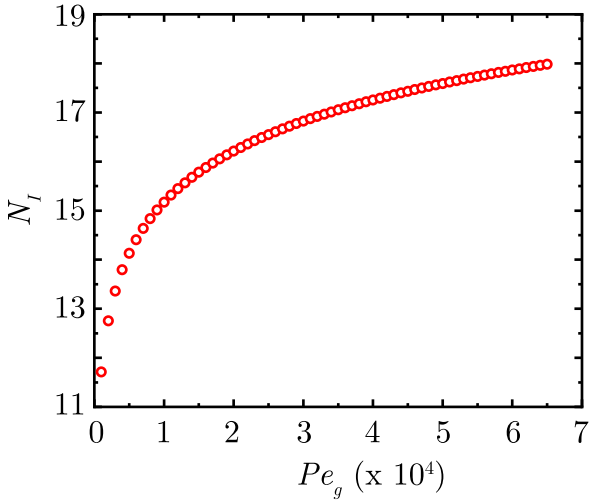

FIGURE 8
Change in position of the inflection point (N_I) with Pe_g. The entire physiological range of Pe_g (based on gas diffusivity and flow rate) is considered.

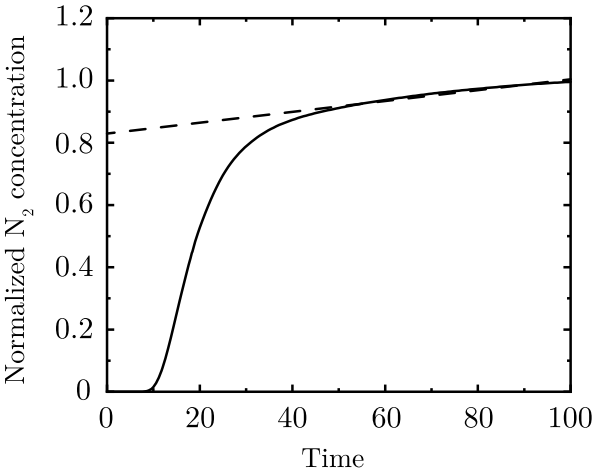

FIGURE 9
Nitrogen washout curve analytically calculated for two asymmetric branches merging. Dashed line represents the "phase III" slope of the washout curve.

of asymmetry or heterogeneity in the lung. A 1D trumpet model, which effectively represents a symmetric lung with well-mixed gas, is known to give a near-zero slope for the alveolar plateau unlike experimental data (Paiva, 1989).

Models with some degree of asymmetric branching are shown to capture the slope of the alveolar plateau (Paiva, 1989; Hasler et al., 2019; Crawford et al., 1985; Engel and Paiva, 1981). This can be understood as follows. During inhalation of pure O_2, the concentration of N_2 in the deeper generations is high and at the mouth it is zero. When exhalation begins, the concentration of N_2 is convected out to the mouth. We can convert the concentration vs. generation number (N) graph during inhalation to the concentration vs. time graph at the mouth during exhalation by the following transformation (see Equation 74). For simplicity, consider the steady state concentration vs. N graph as the limiting profile during inhalation. The transformation basically finds the time t_e it will take for the gas at location x_e to reach the mouth:

$$N_e = \frac{\ln\left[1 - \frac{(1-\alpha)\ln(2\alpha\beta)}{\alpha\ln\alpha}\left(\frac{Qt_e}{A_0L_0}\right)\right]}{\ln(2\alpha\beta)}. \quad (74)$$

Using this transformation, the concentration vs. N graph for N_2 during inhalation is converted to concentration vs. time for N_2 at the mouth during exhalation. Now imagine the whole lung to be composed of two asymmetric branches with different Peclet numbers. Model each branch as a 1D trumpet. The trumpet model solution is applicable for each branch. The N_2 concentration coming out of each branch is mixed at the junction during exhalation. Upon analytically adding the N_2 concentration exhaled from each branch, the slope of the alveolar plateau is recovered as seen in Figure 9. This slope arises due to the superposition of the convective and diffusive portions of the concentration profiles in the two branches (Crawford et al., 1985; Engel and Paiva, 1981). Models with more levels of branching will allow resolution of the phenomenon with greater fidelity (Hasler et al., 2019).

5.6 Clinical relevance

The 1D models of droplet and particle transport discussed in this article (Sections 2 and 3) have been utilised to computationally study pulmonary drug delivery and retention (Chakravarty et al., 2022) with major focus on identifying physiological conditions conducive for delivering drugs to the deep lung. This is crucial for achieving systemic drug delivery. Salient results have been discussed in Section 2.3 using Supplementary Figures S6, S7. Drug delivery efficacy to the deep lung is observed to remain highest for 1 – 5μm aerosols. Drug deposition in the deep lung is observed to increase by a factor of 2, with respect to normal breathing, with doubling of the breathing time period (Chakravarty et al., 2022). This suggests that breath control may be utilised as for enhancing drug delivery efficacy to the deep lung. Inhaled drug load reduces with increase in efficacy which can help in minimizing the side effects associated with drug inhalation.

The pathogen transport model (Section 4.1), coupled with the droplet transport (Section 2.3) and immune response models (Section 4.2), can be utilised to study the spatio-temporal progression of infection within the lung. Chakravarty et al. (2023) utilised this model for understanding SARS-CoV-2 spread to the deep lung and proposed a new paradigm for this propagation called Reaerosolisation of Nasopharyngeal Mucosa (RNM). The model predicted that a severe infection (leading to pneumonia) develops within the deep lung within 2.5–7 days of symptom onset, in agreement with clinical findings. It was observed that immune responses, particularly antibodies and T-lymphocytes, play a critical role in preventing a severe infection. This also reinforces the role played by vaccination in managing a severe infection. The analysis also revealed that managing aerosolization of infected nasopharyngeal mucosa can be used as a potential strategy for minimizing infection spread and severity within the lung. These results have been discussed in Section 4.3 utilising Supplementary Figures S8-S10.

6 Outlook

6.1 Improvement of 1D models and disease specific modeling

1D models discussed in this perspective rely on reduced-order forms of various physical mechanisms (such as particle deposition). Similarly, a better understanding of aerosolization within the airways will help develop aerosolization source terms for use in the 1D governing equations. Aerosolization may take place due to mucosal layer bridge formation within small airways in the deep lung ("airway closure mechanism") (Grotberg, 2011). A second route through shear layer atomization of the mucosal layer during coughing has been reproduced via simulations (Pairetti et al., 2021; Saha et al., 2024) and experiments (Kant et al., 2023). Although mucosal shear flow during normal breathing is stable, increased exhaled aerosol formation during SARS-CoV-2 infection has been reported (Edwards et al., 2021). In addition, shear flows of viscoelastic fluids (such as airway mucus) that are linearly stable have been found to be non-linearly unstable in the presence of large perturbations (Datta et al., 2022). Thus, non-linear stability of the mucosal layer that is driven (and disturbed) by ciliary beating needs further investigation as a potential source of aerosolization.

The need for better aerosolization models is particularly important in the context of SARS-CoV-2 specific modeling since mucosal aerosolization might be significantly enhanced in SARS-CoV-2 patients (Edwards et al., 2021; Pairetti et al., 2021; Morawska et al., 2022; Darquenne et al., 2022a). This requires information on how does SARS-CoV-2 (and other respiratory infections in general) impact mucosal layer viscoelastic properties, and how does that impact the degree of aerosolization within the airways and in the nasopharyngeal region? How would that impact aerosol transport in the airways and would it increase the chances of deep lung infection as seen in SARS-CoV-2 patients? These questions remain unanswered.

Another well-known airborne infection is pulmonary tuberculosis (TB) which continues to be a global menace. Sparse data are available regarding the mechanism underlying the occurrence of TB infection, wherein it is intriguing as to why only 70% of individuals exposed do not get infected, whereas only 30% develop infection (Sharma et al., 2005; Sharma and Mohan, 2017). Thus, careful experiments and fluid dynamics calculations would be important tools to gain these insights.

6.2 Generalization to tree network

Throughout this perspective, the 1D trumpet model is used to represent the entire lung and model different aspects. Several key insights into lung physiology have been reported through the years using this approach. While all aspects of lung physiology may not be captured by a 1D trumpet model for the entire lung (e.g., N_2 washout), there is scope for generalization. The 1D governing equations need not be used to represent the entire lung. Instead 1D equations could be used to represent branches or collection of branches in the lung tree network. Thus, modeling with various degrees of resolution could be done to gain more resolved insights into the physiology of a heterogeneous lung (Hasler et al., 2019). In this direction, stochastic multi-path models of varying granularity has been the focus of one of our groups (Panchagnula) and have yielded significant insights.

6.3 A virtual disease landscape

In this perspective, the 1D governing equations were presented in terms of non-dimensional numbers. These represent the fundamental parameters or metrics on which lung physiology would depend. Consequently, normal or pathological patient groups should occupy different regions in this parameter space defining a *virtual disease landscape* (VDL). The existence of a VDL was shown for esophageal function in one of our groups (Patankar) (Halder et al., 2022) and should be explored in the future for the lungs. The non-dimensional numbers defining the VDL could be utilised as a systematic set of metrics or physiomarkers for disease classification and diagnosis, as was shown for esophageal diseases (Zhao et al., 2023). This can help get mechanistic insights into pathologies. Disease progression could be tracked on the VDL, which coupled with machine learning techniques could be a powerful tool to predict future trajectory of diseases. Finally, the changes in physics-based parameters could be associated with biochemical alteration in the lungs. This connection between functional parameters space to the biochemical space can provide deeper insights into pathogenesis.

6.4 Hybrid diagnostics tools

Measuring the non-dimensional numbers on a patient specific basis to define the "mechanical health" of the lungs in the VDL remains a biomechanics challenge in clinical diagnostics. Reduced-order 1D models coupled with physiologic data from diagnostic tools and machine learning techniques could help measure the physiomarkers (e.g., non-dimensional numbers) for disease classification and diagnosis (Halder et al., 2021; Halder et al., 2022; Halder et al., 2023). This technology could potentially help personalize patient care and treatment planning. Improved and suitably generalized 1D modeling could be an important tool in developing novel physics-machine-learning-clinical-data-based hybrid platforms that could be deployed at point-of-care.

Data availability statement

The original contributions presented in the study are included in the article/Supplementary Material, further inquiries can be directed to the corresponding author.

Author contributions

AC: Formal Analysis, Methodology, Writing – original draft, Writing – review and editing, Software, Conceptualization. DK: Methodology, Writing – review and editing, Software. MP: Formal Analysis, Conceptualization, Writing – review and editing, Methodology. AM: Conceptualization, Writing – review and editing. NP: Formal Analysis, Writing – original draft, Conceptualization, Writing – review and editing, Methodology.

Funding

The author(s) declare that financial support was received for the research and/or publication of this article. The study was partially funded by Sri Balaji Arogya Vara Prasadini (SBAVP) scheme of Sri Venkateswara Institute of Medical Sciences, Tirupati, Tirumala Tirupati Devasthanams, Tirupati (Grant No. Faculty/ERPW/28/2016-17). DK would like to acknowledge the Prime Minister's Research Fellows (PMRF) scheme, Ministry of Education, Government of India (project no. SB21221950 AMPMRF008445) for providing fellowship.

Conflict of interest

The authors declare that the research was conducted in the absence of any commercial or financial relationships that could be construed as a potential conflict of interest.

Generative AI statement

The author(s) declare that no Generative AI was used in the creation of this manuscript.

Any alternative text (alt text) provided alongside figures in this article has been generated by Frontiers with the support of artificial intelligence and reasonable efforts have been made to ensure accuracy, including review by the authors wherever possible. If you identify any issues, please contact us.

Publisher's note

Supplementary material

The Supplementary Material for this article can be found online at: https://www.frontiersin.org/articles/10.3389/fphys.2025.1635983/full#supplementary-material

References

Abkarian, M., and Stone, H. (2020). Stretching and break-up of saliva filaments during speech: a route for pathogen aerosolization and its potential mitigation. *Phys. Rev. Fluids* 5, 102301. doi:10.1103/physrevfluids.5.102301

Abkarian, M., Mendez, S., Xue, N., Yang, F., and Stone, H. A. (2020). Speech can produce jet-like transport relevant to asymptomatic spreading of virus. *Proc. Natl. Acad. Sci.* 117, 25237–25245. doi:10.1073/pnas.2012156117

Anzai, H., Shindo, Y., Kohata, Y., Hasegawa, M., Takana, H., Matsunaga, T., et al. (2022). Coupled discrete phase model and eulerian wall film model for numerical simulation of respiratory droplet generation during coughing. *Sci. Rep.* 12, 14849. doi:10.1038/s41598-022-18788-3

Atzori, M., Gallorini, E., Cottini, C., Benassi, A., and Quadrio, M. (2025). Direct numerical simulations of inhalation in a 23-generation lung model. *arXiv Prepr. arXiv:2506.14729*. doi:10.48550/arXiv.2506.14729

Baccam, P., Beauchemin, C., Macken, C. A., Hayden, F. G., and Perelson, A. S. (2006). Kinetics of influenza a virus infection in humans. *J. virology* 80, 7590–7599. doi:10.1128/JVI.01623-05

Banerji, R., Grifno, G. N., Shi, L., Smolen, D., LeBourdais, R., Muhvich, J., et al. (2023). Crystal ribcage: a platform for probing real-time lung function at cellular resolution. *Nat. methods* 20, 1790–1801. doi:10.1038/s41592-023-02004-9

Bartol, I. R., Graffigna Palomba, M. S., Tano, M. E., and Dewji, S. A. (2024). Computational multiphysics modeling of radioactive aerosol deposition in diverse human respiratory tract geometries. *Commun. Eng.* 3, 152. doi:10.1038/s44172-024-00296-z

Basu, S. (2021). Computational characterization of inhaled droplet transport to the nasopharynx. *Sci. Rep.* 11, 1–13. doi:10.1038/s41598-021-85765-7

Basu, S., Holbrook, L. T., Kudlaty, K., Fasanmade, O., Wu, J., Burke, A., et al. (2020). Numerical evaluation of spray position for improved nasal drug delivery. *Sci. Rep.* 10, 10568–18. doi:10.1038/s41598-020-66716-0

Basu, S., Akash, M. M. H., Hochberg, N. S., Senior, B. A., Joseph-McCarthy, D., and Chakravarty, A. (2022). From sars-cov-2 infection to covid-19 morbidity: an *in silico* projection of virion flow rates to the lower airway *via* nasopharyngeal fluid boluses. *Rhinol. Online* 5, 10–18. doi:10.4193/rhinol/21.053

Ben-Tal, A. (2006). Simplified models for gas exchange in the human lungs. *J. Theor. Biol.* 238, 474–495. doi:10.1016/j.jtbi.2005.06.005

Biswas, R., Pal, A., Pal, R., Sarkar, S., and Mukhopadhyay, A. (2022). Risk assessment of covid infection by respiratory droplets from cough for various ventilation scenarios inside an elevator: an openfoam-based computational fluid dynamics analysis. *Phys. Fluids* 34, 013318. doi:10.1063/5.0073694

Bourouiba, L. (2021). The fluid dynamics of disease transmission. *Annu. Rev. Fluid Mech.* 53, 473–508. doi:10.1146/annurev-fluid-060220-113712

Cao, P., Yan, A. W., Heffernan, J. M., Petrie, S., Moss, R. G., Carolan, L. A., et al. (2015). Innate immunity and the inter-exposure interval determine the dynamics of secondary influenza virus infection and explain observed viral hierarchies. *PLoS Comput. Biol.* 11, e1004334. doi:10.1371/journal.pcbi.1004334

Chakravarty, A., Patankar, N. A., and Panchagnula, M. V. (2019). Aerosol transport in a breathing alveolus. *Phys. Fluids* 31, 121901. doi:10.1063/1.5127787

Chakravarty, A., Panchagnula, M. V., Mohan, A., and Patankar, N. A. (2022). Pulmonary drug delivery and retention: a computational study to identify plausible parameters based on a coupled airway-mucus flow model. *PLOS Comput. Biol.* 18, e1010143. doi:10.1371/journal.pcbi.1010143

Chakravarty, A., Panchagnula, M. V., and Patankar, N. (2023). Inhalation of virus-loaded droplets as a clinically plausible pathway to deep lung infection. *Front. Physiology* 14, 1073165. doi:10.3389/fphys.2023.1073165

Chen, A., Wessler, T., Daftari, K., Hinton, K., Boucher, R. C., Pickles, R., et al. (2022). Modeling insights into sars-cov-2 respiratory tract infections prior to immune protection. *Biophysical J.* 121, 1619–1631. doi:10.1016/j.bpj.2022.04.003

Chen, L., Yousaf, M., Xu, J., Ma, X., Zhou, X., Li, G., et al. (2025). Ultrafine particles deposition in human respiratory tract: experimental measurement and modeling. *Ecotoxicol. Environ. Saf.* 295, 118123. doi:10.1016/j.ecoenv.2025.118123

Choi, J.-I., and Kim, C. S. (2007). Mathematical analysis of particle deposition in human lungs: an improved single path transport model. *Inhal. Toxicol.* 19, 925–939. doi:10.1080/08958370701513014

Crawford, A., Makowska, M., Paiva, M., and Engel, L. (1985). Convection-and diffusion-dependent ventilation maldistribution in normal subjects. *J. Appl. Physiology* 59, 838–846. doi:10.1152/jappl.1985.59.3.838

Cu, Y., and Saltzman, W. M. (2009). Mathematical modeling of molecular diffusion through mucus. *Adv. drug Deliv. Rev.* 61, 101–114. doi:10.1016/j.addr.2008.09.006

Darquenne, C., and Paiva, M. (1994). One-dimensional simulation of aerosol transport and deposition in the human lung. *J. Appl. Physiology* 77, 2889–2898. doi:10.1152/jappl.1994.77.6.2889

Darquenne, C., Borojeni, A. A., Colebank, M. J., Forest, M. G., Madas, B. G., Tawhai, M., et al. (2022a). Aerosol transport modeling: the key link between lung infections of individuals and populations. *Front. Physiology* 13, 923945. doi:10.3389/fphys.2022.923945

Darquenne, C., Theilmann, R. J., Fine, J. M., and Verbanck, S. A. (2022b). Nitrogen-based lung clearance index: a valid physiological biomarker for the clinic. *J. Appl. Physiology* 132, 1290–1296. doi:10.1152/japplphysiol.00511.2021

Datta, S. S., Ardekani, A. M., Arratia, P. E., Beris, A. N., Bischofberger, I., McKinley, G. H., et al. (2022). Perspectives on viscoelastic flow instabilities and elastic turbulence. *Phys. Rev. fluids* 7, 080701. doi:10.1103/physrevfluids.7.080701

Deepa, M., Vidhyapriya, R., and Raagul, A. (2025). A novel breath pattern model and analysis to minimize patient discomfort in medical ventilators. *Sci. Rep.* 15, 2075. doi:10.1038/s41598-025-86187-5

Devi, S. K., Panchagnula, M. V., and Alladi, M. (2016). Designing aerosol size distribution to minimize inter-subject variability of alveolar deposition. *J. Aerosol Sci.* 101, 144–155. doi:10.1016/j.jaerosci.2016.08.005

Dobrovolny, H. M., Reddy, M. B., Kamal, M. A., Rayner, C. R., and Beauchemin, C. A. (2013). Assessing mathematical models of influenza infections using features of the immune response. *PloS one* 8, e57088. doi:10.1371/journal.pone.0057088

Edwards, D. A., Ausiello, D., Salzman, J., Devlin, T., Langer, R., Beddingfield, B. J., et al. (2021). Exhaled aerosol increases with COVID-19 infection, age, and obesity. *Proc. Natl. Acad. Sci.* 118, e2021830118. doi:10.1073/pnas.2021830118

Engel, L., and Paiva, M. (1981). Analyses of sequential filling and emptying of the lung. *Respir. Physiol.* 45, 309–321. doi:10.1016/0034-5687(81)90014-1

Fishler, R., Hofemeier, P., Etzion, Y., Dubowski, Y., and Sznitman, J. (2015). Particle dynamics and deposition in true-scale pulmonary acinar models. *Sci. Rep.* 5, 14071. doi:10.1038/srep14071

Florens, M., Sapoval, B., and Filoche, M. (2011). Optimal branching asymmetry of hydrodynamic pulsatile trees. *Phys. Rev. Lett.* 106, 178104. doi:10.1103/PhysRevLett.106.178104

Foster, W., Langenback, E., and Bergofsky, E. (1980). Measurement of tracheal and bronchial mucus velocities in man: relation to lung clearance. *J. Appl. Physiology* 48, 965–971. doi:10.1152/jappl.1980.48.6.965

Ghorui, S., Kundu, D., Chakravarty, A., and Panchagnula, M. V. (2024). The impact of asymmetric branching on particle deposition in conducting airways. *Int. J. Multiph. Flow* 179, 104935. doi:10.1016/j.ijmultiphaseflow.2024.104935

Grant, R. A., Morales-Nebreda, L., Markov, N. S., Swaminathan, S., Querrey, M., Guzman, E. R., et al. (2021). Circuits between infected macrophages and T cells in SARS-CoV-2 pneumonia. *Nature* 590, 635–641. doi:10.1038/s41586-020-03148-w

Grotberg, J. B. (2011). Respiratory fluid mechanics. *Phys. fluids* 23, 021301. doi:10.1063/1.3517737

Guha, A. (2008). Transport and deposition of particles in turbulent and laminar flow. *Annu. Rev. Fluid Mech.* 40, 311–341. doi:10.1146/annurev.fluid.40.111406.102220

Hagman, K., Hedenstierna, M., Gille-Johnson, P., Hammas, B., Grabbe, M., Dillner, J., et al. (2020). Sars-cov-2 rna in serum as predictor of severe outcome in covid-19: a retrospective cohort study. *Clin. Infect. Dis.* 2020, 1285. doi:10.1093/cid/ciaa1285

Halder, S., Acharya, S., Kou, W., Kahrilas, P. J., Pandolfino, J. E., and Patankar, N. A. (2021). Mechanics informed fluoroscopy of esophageal transport. *Biomechanics Model. Mechanobiol.* 20, 925–940. doi:10.1007/s10237-021-01420-0

Halder, S., Yamasaki, J., Acharya, S., Kou, W., Elisha, G., Carlson, D. A., et al. (2022). Virtual disease landscape using mechanics-informed machine learning: application to esophageal disorders. *Artif. Intell. Med.* 134, 102435. doi:10.1016/j.artmed.2022.102435

Halder, S., Johnson, E. M., Yamasaki, J., Kahrilas, P. J., Markl, M., Pandolfino, J. E., et al. (2023). Mri-mech: mechanics-informed mri to estimate esophageal health. *Front. Physiology* 14, 1195067. doi:10.3389/fphys.2023.1195067

Hamed, R., Schenck, D. M., and Fiegel, J. (2020). Surface rheological properties alter aerosol formation from mucus mimetic surfaces. *Soft Matter* 16, 7823–7834. doi:10.1039/d0sm01232g

Harrison, A. G., Lin, T., and Wang, P. (2020). Mechanisms of sars-cov-2 transmission and pathogenesis. *Trends Immunol.* 41, 1100–1115. doi:10.1016/j.it.2020.10.004

Haslbeck, K., Schwarz, K., Hohlfeld, J. M., Seume, J. R., and Koch, W. (2010). Submicron droplet formation in the human lung. *J. aerosol Sci.* 41, 429–438. doi:10.1016/j.jaerosci.2010.02.010

Hasler, D., Anagnostopoulou, P., Nyilas, S., Latzin, P., Schittny, J., and Obrist, D. (2019). A multi-scale model of gas transport in the lung to study heterogeneous lung ventilation during the multiple-breath washout test. *PLoS Comput. Biol.* 15, e1007079. doi:10.1371/journal.pcbi.1007079

He, S., Gui, J., Xiong, K., Chen, M., Gao, H., and Fu, Y. (2022). A roadmap to pulmonary delivery strategies for the treatment of infectious lung diseases. *J. nanobiotechnology* 20, 101. doi:10.1186/s12951-022-01307-x

Heyder, J., Gebhart, J., Rudolf, G., Schiller, C. F., and Stahlhofen, W. (1986). Deposition of particles in the human respiratory tract in the size range 0.005-15 μm. *J. aerosol Sci.* 17, 811–825. doi:10.1016/0021-8502(86)90035-2

Hofmann, W. (2011). Modelling inhaled particle deposition in the human Lung—A review. *J. Aerosol Sci.* 42, 693–724. doi:10.1016/j.jaerosci.2011.05.007

Kant, P., Pairetti, C., Saade, Y., Popinet, S., Zaleski, S., and Lohse, D. (2023). Bag-mediated film atomization in a cough machine. *Phys. Rev. Fluids* 8, 074802. doi:10.1103/physrevfluids.8.074802

Karamaoun, C., Sobac, B., Mauroy, B., Van Muylem, A., and Haut, B. (2018). New insights into the mechanisms controlling the bronchial mucus balance. *PloS One* 13, e0199319. doi:10.1371/journal.pone.0199319

Kassinos, S. C., and Sznitman, J. (2025). Multiscale modeling of respiratory transport phenomena and intersubject variability. *Annu. Rev. Fluid Mech.* 57, 141–165. doi:10.1146/annurev-fluid-031424-103721

Kim, C. S., and Jaques, P. A. (2004). Analysis of total respiratory deposition of inhaled ultrafine particles in adult subjects at various breathing patterns. *Aerosol Sci. Technol.* 38, 525–540. doi:10.1080/02786820490465513

Kleinstreuer, C., and Zhang, Z. (2010). Airflow and particle transport in the human respiratory system. *Annu. Rev. fluid Mech.* 42, 301–334. doi:10.1146/annurev-fluid-121108-145453

Kou, J., Chen, Y., Zhou, X., Lu, H., Wu, F., and Fan, J. (2014). Optimal structure of tree-like branching networks for fluid flow. *Phys. A* 393, 527–534. doi:10.1016/j.physa.2013.08.029

Koullapis, P., Kassinos, S. C., Bivolarova, M. P., and Melikov, A. K. (2016). Particle deposition in a realistic geometry of the human conducting airways: effects of inlet velocity profile, inhalation flowrate and electrostatic charge. *J. biomechanics* 49, 2201–2212. doi:10.1016/j.jbiomech.2015.11.029

Koullapis, P., Hofemeier, P., Sznitman, J., and Kassinos, S. C. (2018a). An efficient computational fluid-particle dynamics method to predict deposition in a simplified approximation of the deep lung. *Eur. J. Pharm. Sci.* 113, 132–144. doi:10.1016/j.ejps.2017.09.016

Koullapis, P., Kassinos, S. C., Muela, J., Perez-Segarra, C., Rigola, J., Lehmkuhl, O., et al. (2018b). Regional aerosol deposition in the human airways: the siminhale benchmark case and a critical assessment of *in silico* methods. *Eur. J. Pharm. Sci.* 113, 77–94. doi:10.1016/j.ejps.2017.09.003

Koullapis, P., Ollson, B., Kassinos, S. C., and Sznitman, J. (2019). Multiscale *in silico* lung modeling strategies for aerosol inhalation therapy and drug delivery. *Curr. Opin. Biomed. Eng.* 11, 130–136. doi:10.1016/j.cobme.2019.11.003

Koullapis, P., Stylianou, F., Sznitman, J., Olsson, B., and Kassinos, S. (2020). Towards whole-lung simulations of aerosol deposition: a model of the deep lung. *J. Aerosol Sci.* 144, 105541. doi:10.1016/j.jaerosci.2020.105541

Krogh, A., and Lindhard, J. (1917). The volume of the dead space in breathing and the mixing of gases in the lungs of man. *J. physiology* 51, 59–90. doi:10.1113/jphysiol.1917.sp001785

Kundu, D., and Panchagnula, M. V. (2023). Asymmetric lung increases particle filtration by deposition. *Sci. Rep.* 13, 9040. doi:10.1038/s41598-023-36176-3

Kundu, D., and Panchagnula, M. V. (2025). Stochastic asymmetric bronchial tree models for population-scale variability in dosimetry. *J. Aerosol Sci.* 189, 106622. doi:10.1016/j.jaerosci.2025.106622

Kuprat, A., Jalali, M., Jan, T., Corley, R., Asgharian, B., Price, O., et al. (2021). Efficient bi-directional coupling of 3d computational fluid-particle dynamics and 1d multiple path particle dosimetry lung models for multiscale modeling of aerosol dosimetry. *J. aerosol Sci.* 151, 105647. doi:10.1016/j.jaerosci.2020.105647

Kuprat, A. P., Price, O., Asgharian, B., Singh, R. K., Colby, S., Yugulis, K., et al. (2023). Automated bidirectional coupling of multiscale models of aerosol dosimetry: validation with subject-specific deposition data. *J. Aerosol Sci.* 174, 106233. doi:10.1016/j.jaerosci.2023.106233

Leung, N. H. (2021). Transmissibility and transmission of respiratory viruses. *Nat. Rev. Microbiol.* 19, 528–545. doi:10.1038/s41579-021-00535-6

Looney, M. R., Thornton, E. E., Sen, D., Lamm, W. J., Glenny, R. W., and Krummel, M. F. (2011). Stabilized imaging of immune surveillance in the mouse lung. *Nat. methods* 8, 91–96. doi:10.1038/nmeth.1543

Majumdar, A., Alencar, A. M., Buldyrev, S. V., Hantos, Z., Lutchen, K. R., Stanley, H. E., et al. (2005). Relating airway diameter distributions to regular branching asymmetry in the lung. *Phys. Rev. Lett.* 95, 168101. doi:10.1103/PhysRevLett.95.168101

Mate-Kole, E. M., Howard, S. C., Golden, A. P., and Dewji, S. A. (2024). Machine learning-enhanced stochastic uncertainty and sensitivity analysis of the icrp human respiratory tract model for an inhaled radionuclide. *J. Radiological Prot.* 44, 041507. doi:10.1088/1361-6498/ad7ec3

Mauroy, B., Filoche, M., Weibel, E., and Sapoval, B. (2004). An optimal bronchial tree May be dangerous. *Nature* 427, 633–636. doi:10.1038/nature02287

Mauroy, B., Fausser, C., Pelca, D., Merckx, J., and Flaud, P. (2011). Toward the modeling of mucus draining from the human lung: role of the geometry of the airway tree. *Phys. Biol.* 8, 056006. doi:10.1088/1478-3975/8/5/056006

Miguel, A. F. (2016). Toward an optimal design principle in symmetric and asymmetric tree flow networks. *J. Theor. Biol.* 389, 101–109. doi:10.1016/j.jtbi.2015.10.027

Miguel, A. F. (2022). An assessment of branching asymmetry of the tracheobronchial tree. *Sci. Rep.* 12, 10145. doi:10.1038/s41598-022-14072-6

Mitsakou, C., Helmis, C., and Housiadas, C. (2005). Eulerian modelling of lung deposition with sectional representation of aerosol dynamics. *J. Aerosol Sci.* 36, 75–94. doi:10.1016/j.jaerosci.2004.08.008

Mittal, R., Ni, R., and Seo, J.-H. (2020). The flow physics of COVID-19. *J. Fluid Mech.* 894, F2. doi:10.1017/jfm.2020.330

Möller, G., Bieber, M., Gürzing, S., Thiebes, A. L., Klein, S., Cornelissen, C. G., et al. (2021). Transparent 23-generation airway model for experimental investigation of aerosol flow and deposition within the human respiratory tract. *J. Aerosol Sci.* 156, 105782. doi:10.1016/j.jaerosci.2021.105782

Morawska, L., Buonanno, G., Mikszewski, A., and Stabile, L. (2022). The physics of respiratory particle generation, fate in the air, and inhalation. *Nat. Rev. Phys.* 4, 723–734. doi:10.1038/s42254-022-00506-7

Napoli, N. J., Rodrigues, V. R., and Davenport, P. W. (2022). Characterizing and modeling breathing dynamics: flow rate, rhythm, period, and frequency. *Front. Physiology* 12, 772295. doi:10.3389/fphys.2021.772295

Néant, N., Lingas, G., Le Hingrat, Q., Ghosn, J., Engelmann, I., Lepiller, Q., et al. (2021). Modeling sars-cov-2 viral kinetics and association with mortality in hospitalized patients from the french covid cohort. *Pro. Nat. Academy Sci.* 118. e2017962118

Neelakantan, S., Xin, Y., Gaver, D. P., Cereda, M., Rizi, R., Smith, B. J., et al. (2022). Computational lung modelling in respiratory medicine. *J. R. Soc. Interface* 19, 20220062. doi:10.1098/rsif.2022.0062

Nunn, J. (1957). Physiological aspects of artificial ventilation. *BJA Br. J. Anaesth.* 29, 540–552. doi:10.1093/bja/29.12.540

Otis, A. B., Fenn, W. O., and Rahn, H. (1950). Mechanics of breathing in man. *J. Appl. physiology* 2, 592–607. doi:10.1152/jappl.1950.2.11.592

Pairetti, C., Villiers, R., and Zaleski, S. (2021). On shear layer atomization within closed channels: numerical simulations of a cough-replicating experiment. *Comput. and Fluids* 231, 105125. doi:10.1016/j.compfluid.2021.105125

Paiva, M. (1973). Gas transport in the human lung. *J. Appl. Physiology* 35, 401–410. doi:10.1152/jappl.1973.35.3.401

Paiva, M. (1989). Pneumologists breathe easy. *Nature* 342, 623. doi:10.1038/342623a0

Paiva, M., and Engel, L. (1981). The anatomical basis for the sloping n2 plateau. *Respir. Physiol.* 44, 325–337. doi:10.1016/0034-5687(81)90027-x

Paiva, M., Lacquet, L., and van der Linden, L. (1976). Gas transport in a model derived from hansen-ampaya anatomical data of the human lung. *J. Appl. Physiology* 41, 115–119. doi:10.1152/jappl.1976.41.1.115

Pal, A., Biswas, R., Pal, R., Sarkar, S., and Mukhopadhyay, A. (2023). A novel approach to preventing sars-cov-2 transmission in classrooms: a numerical study. *Phys. Fluids* 35, 013308. doi:10.1063/5.0131672

Pedley, T. (1977). Pulmonary fluid dynamics. *Annu. Rev. Fluid Mech.* 9, 229–274. doi:10.1146/annurev.fl.09.010177.001305

Popel, A. S. (1980). A model of pressure and flow distribution in branching networks. *J. Appl. Mech.* 47, 247–253. doi:10.1115/1.3153650

Pradhan, K., and Guha, A. (2019). Fluid dynamics of oscillatory flow in three-dimensional branching networks. *Phys. Fluids* 31, 063601. doi:10.1063/1.5093724

Quirouette, C., Younis, N. P., Reddy, M. B., and Beauchemin, C. A. (2020). A mathematical model describing the localization and spread of influenza A virus infection within the human respiratory tract. *PLOS Comput. Biol.* 16, e1007705. doi:10.1371/journal.pcbi.1007705

Raabe, O. (1976). *Tracheobronchial geometry-human, dog, rat, hamster*. Lovelace Foundation for Medical Education and Research.

Ravi, V. R., Korkmaz, F. T., De Ana, C. L., Lu, L., Shao, F.-Z., Odom, C. V., et al. (2025). Lung cd4+ resident memory t cells use airway secretory cells to stimulate and regulate onset of allergic airway neutrophilic disease. *Cell Rep.* 44, 115294. doi:10.1016/j.celrep.2025.115294

Saha, S., Manna, M. K., Chakravarty, A., Sarkar, S., Mukhopadhyay, A., and Sen, S. (2024). Insights into the fluid dynamics of bioaerosol formation in a model respiratory tract. *Biomicrofluidics* 18, 054106. doi:10.1063/5.0219332

Sapoval, B., Filoche, M., and Weibel, E. (2002). Smaller is better – but not too small: a physical scale for the design of the mammalian pulmonary acinus. *Proc. Natl. Acad. Sci.* 99, 10411–10416. doi:10.1073/pnas.122352499

Sharma, S. K., and Mohan, A. (2017). *Miliary Tuberculosis*. John Wiley Sons, Ltd, 491–513. doi:10.1128/9781555819866.ch29

Sharma, S. K., Mohan, A., Sharma, A., and Mitra, D. K. (2005). Miliary tuberculosis: new insights into an old disease. *Lancet Infect. Dis.* 5, 415–430. doi:10.1016/S1473-3099(05)70163-8

Smith, D., Gaffney, E., and Blake, J. (2008). Modelling mucociliary clearance. *Respir. Physiology and Neurobiol.* 163, 178–188. doi:10.1016/j.resp.2008.03.006

Soni, B., Miguel, A. F., and Kumar Nayak, A. (2020). A mathematical analysis for constructal design of tree flow networks under unsteady flow. *Proc. R. Soc. A* 476, 20200377. doi:10.1098/rspa.2020.0377

Sznitman, J. (2013). Respiratory microflows in the pulmonary acinus. *J. Biomechanics* 46, 284–298. doi:10.1016/j.jbiomech.2012.10.028

Sznitman, J. (2021). Revisiting airflow and aerosol transport phenomena in the deep lungs with microfluidics. *Chem. Rev.* 122, 7182–7204. doi:10.1021/acs.chemrev.1c00621

Tan, C., Li, S., Liang, Y., Chen, M., and Liu, J. (2020). SARS-CoV-2 viremia may predict rapid deterioration of COVID-19 patients. *Braz. J. Infect. Dis.* 24, 565–569. doi:10.1016/j.bjid.2020.08.010

Taulbee, D. B., and Yu, C. (1975). A theory of aerosol deposition in the human respiratory tract. *J. Appl. Physiology* 38, 77–85. doi:10.1152/jappl.1975.38.1.77

Tawhai, M. H., Hunter, P., Tschirren, J., Reinhardt, J., McLennan, G., and Hoffman, E. A. (2004). Ct-based geometry analysis and finite element models of the human and ovine bronchial tree. *J. Appl. physiology* 97, 2310–2321. doi:10.1152/japplphysiol.00520.2004

Tsuda, A., Henry, F. S., and Butler, J. P. (2008). Gas and aerosol mixing in the acinus. *Respir. physiology and Neurobiol.* 163, 139–149. doi:10.1016/j.resp.2008.02.010

Wang, J.-Y., Suddards, M., Mellor, C., and Owers-Bradley, J. (2013). Lung function measurement with multiple-breath-helium washout system. *Med. Eng. and Phys.* 35, 457–469. doi:10.1016/j.medengphy.2012.06.010

Wang, S., Pan, Y., Wang, Q., Miao, H., Brown, A. N., and Rong, L. (2020). Modeling the viral dynamics of sars-cov-2 infection. *Math. Biosci.* 328, 108438. doi:10.1016/j.mbs.2020.108438

Wang, C. C., Prather, K. A., Sznitman, J., Jimenez, J. L., Lakdawala, S. S., Tufekci, Z., et al. (2021). Airborne transmission of respiratory viruses. *Science* 373, eabd9149. doi:10.1126/science.abd9149

Weibel, E., and Gomez, D. (1962). Architecture of the human lung. Use of quantitative methods establishes fundamental relations between size and number of lung structures. *Science* 137, 577–585. doi:10.1126/science.137.3530.577

Weibel, E. R., Cournand, A. F., and Richards, D. W. (1963) *Morphometry of the human lung*, 1. Springer.

West, J. B. (2012). *Respiratory physiology: the essentials*. Lippincott Williams and Wilkins.

Wiersinga, W. J., Rhodes, A., Cheng, A. C., Peacock, S. J., and Prescott, H. C. (2020). Pathophysiology, transmission, diagnosis, and treatment of coronavirus disease 2019 (COVID-19): a review. *JAMA* 324, 782–793. doi:10.1001/jama.2020.12839

Yeates, D., Aspin, N., Levison, H., Jones, M., and Bryan, A. (1975). Mucociliary tracheal transport rates in man. *J. Appl. physiology* 39, 487–495. doi:10.1152/jappl.1975.39.3.487

Yeh, H.-C., and Schum, G. (1980). Models of human lung airways and their application to inhaled particle deposition. *Bull. Math. Biol.* 42, 461–480. doi:10.1007/BF02460796

Zhang, X., Li, F., Rajaraman, P. K., Choi, J., Comellas, A. P., Hoffman, E. A., et al. (2022). A computed tomography imaging-based subject-specific whole-lung deposition model. *Eur. J. Pharm. Sci.* 177, 106272. doi:10.1016/j.ejps.2022.106272

Zhao, T. Y., Johnson, E. M., Elisha, G., Halder, S., Smith, B. C., Allen, B. D., et al. (2023). Blood–wall fluttering instability as a physiomarker of the progression of thoracic aortic aneurysms. *Nat. Biomed. Eng.* 7, 1614–1626. doi:10.1038/s41551-023-01130-1